This article has been published in J Mech Behav Biomed Mater. 2016 May 14; 62:247-267. doi:10.1016/j.jmbbm.2016.05.013.

Title: Advanced zinc-doped adhesives for high performance at the resin-carious dentin interface.

Short title: Bioactivity of etch-and-rinse Zn-doped at the resin/carious dentin interfaces.

Authors: Manuel Toledano[1*], Raquel Osorio[1], Estrella Osorio[1], Franklin García-Godoy[2], Manuel Toledano-Osorio[1], Fátima S. Aguilera[1].

Institution: [1]University of Granada, Faculty of Dentistry, Dental Materials Section.
[2]Bioscience Research Center, College of Dentistry, University of Tennessee, Health Science Center, 875 Union Avenue.

Address: [1]University of Granada, Faculty of Dentistry, Dental Materials Section.
Colegio Máximo de Cartuja s/n,
18071 – Granada - Spain.

*Corresponding author: Prof. Manuel Toledano
University of Granada, Faculty of Dentistry
Dental Materials Section
Colegio Máximo de Cartuja s/n
18071 – Granada - Spain.
Tel.: +34-958243788
Fax: +34-958240809
Email: toledano@ugr.es

ABSTRACT

The purpose of this study was to evaluate the remineralization ability of an etch-and-rinse Zn-doped resin applied on caries-affected dentin (CAD). CAD surfaces were subjected to: i) 37% phosphoric acid (PA) or ii) 0.5 M ethylenediaminetetraacetic acid (EDTA). 10 wt% ZnO nanoparticles or 2 wt% $ZnCl_2$ were added into the adhesive Single Bond (SB), to create the following groups: PA+SB, PA+SB-ZnO, PA+SB-$ZnCl_2$, EDTA+SB, EDTA+SB-ZnO, EDTA+SB-$ZnCl_2$. Bonded interfaces were submitted to mechanical loading or stored during 24 h. Remineralization of the bonded interfaces was studied by AFM nano-indentation (hardness and Young's modulus), Raman spectroscopy [mapping with principal component analysis (PCA), and hierarchical cluster analysis (HCA)] and Masson's trichrome staining technique. Dentin samples treated with PA+SB-ZnO attained the highest values of nano-mechanical properties. Load cycling increased both mineralization and crystallographic maturity at the interface; this effect was specially noticed when using $ZnCl_2$-doped resin in EDTA-treated carious dentin. Crosslinking attained higher frequencies indicating better conformation and organization of collagen in specimens treated with PA+SB-ZnO, after load cycling. Trichrome staining technique depicted a deeper demineralized dentin fringe that became reduced after loading, and it was not observable in EDTA+SB groups. Multivariate analysis confirmed de homogenizing effect of load cycling in the percentage of variances, traces of centroids and distribution of clusters, especially in specimens treated with EDTA+SB-$ZnCl_2$.

Key words: Caries, dentin, remineralization, load cycling, Zn-doped adhesives, Raman.

1. INTRODUCTION

Sound dentin is mainly composed of type I collagen fibrils with associated non-collagenous proteins, forming a three-dimensional matrix that is reinforced by mineral (Bertassoni et al., 2009), but non carious dentin is not the substrate most frequently involved in clinical dentistry. Instead, dentists usually must bond adhesives to irregular dentin substrates such as carious dentin (Wang et al., 2007). Carious dentin consists of a superficial opaque zone of caries-infected dentin and a deeper transparent zone of caries-affected dentin (CAD) (Fusayama et al., 1979), located adjacent to the intact dentin. CAD is partially demineralized and more porous than non-carious dentin with a predominantly intact collagen matrix. It should be preserved during clinical treatment because it is remineralizable and serves as a suitable substrate for dentin adhesion (Yoshiyama et al., 2000), but to date, there is relatively limited information about bonding to this clinically relevant substrate (Haj-Ali et al., 2006; Marangos et al., 2009).

'Etch-and-rinse' adhesives represent the golden standard in adhesive dentistry and involve a separate etch-and-rinse phase before the application of the adhesive. In their most common configuration, phosphoric acid (PA) is applied to demineralize the underlying dentin (De Munck et al., 2005; Osorio et al., 2005), and then, rinsed off. The conditioning step is followed by a priming step and application of the adhesive resin. This interface has been called hybrid layer (HL), made of resin and collagen (Nakabayashi, 1992; Wang and Spencer, 2003). The ideal hybrid layer would be characterized as a three-dimensional collagen-resin biopolymer that provides both a continuous and stable link between the bulk adhesive and dentin substrate (Misra et al., 2004), but a volume of demineralized/unprotected collagen remains at the bottom of the hybrid layer (BHL). This unprotected collagen may become the sites for collagen

hydrolysis by host-derived matrix metalloproteinases (MMPs) enzymes (Osorio et al., 2011a).

During caries progression, intermitent pH fluctuations are produced and will permit MMPs activation (at acidic conditions) and MMPs action (at neutral pH) (Bertini et al., 2012; Chaussain-Miller et al., 2006), promoting MMPs-mediated collagen degradation. The more intense expression of MMPs in CAD *vs.* sound dentin (Toledano et al., 2010) explains why hybrid layers created in CAD degraded much faster (6 months *vs.* 14 moths) than those created by the same etch-and-rinse adhesive in sound, intact dentin (Carrilho et al., 2007). Milder conditioners (*i.e.* EDTA) eliminate the smear layer and plugs, but removing less amount of calcium from dentin surface, promoting shallow demineralization on this previous demineralized substrate (CAD) and inducing favorable chemical modifications (Toledano et al., 2014a). Nevertheless, even with EDTA agents, it seems that a volume of demineralized and non-resin infiltrated collagen remains at the bottom of the hybrid layer (Spencer and Wang, 2001).

If effective inhibitors of MMPs are included in resin-dentin bonding interfaces, they may protect the seed crystallite-sparse collagen fibrils of the scaffold from degradation, and they could be remineralized (Liu et al., 2011). Reincorporation of mineral into the demineralized dentin matrix is important since the mineral precipitated may work as a constant site for further nucleation, and the remineralized subsurface of the tissue may be more resistant to subsequent acid attack. Zinc has been demonstrated to reduce MMPs-mediated collagen degradation (Osorio et al., 2011b), to inhibit dentin demineralization (Takatsuka et al., 2005) and to induce dentin remineralization at the bonded interface (Toledano et al., 2013). Zinc influences signaling pathways and stimulates a metabolic effect in hard tissue mineralization (Hoppe et al., 2011) and remineralization processes (Lynch et al., 2011). Zinc elicits a specific biological

response at the interface of the material which results in the formation of a bond between tissue and material (Kokubo et al., 1990).

Remineralization of caries-affected dentin has, as its ultimate goal, the re-establishment of the functionality of the affected tissue, which can be described as the competence of the dentin in accomplishing its role in the tooth. Simple precipitation of mineral into the loose demineralized dentin matrix may be of relatively high mineral content, but low mechanical properties, misleading information on the actual effectiveness of the remineralization approaches (Xu et al., 2013).

Ideally, a restoration should not only be able to chemically bond to the tooth structure, but must also behave mechanically like tooth itself in the oral environment, especially when subjected to mastication (Angker and Swain, 2006; Frankenberger et al., 2005). Dentin mineral is composed by carbonate-substituted calcium hydroxyapatite crystals and magnesium organized in a crystal lattice; this lattice structure affords the mechanical properties of the healthy and carious tissue. Nano-indentation has recently been used for the examination of tooth structure, measuring both hardness and elastic modulus (Kinney et al., 2005).

The mechanical behavior of the resin-dentin interface is an important aspect contributing to the outstanding durability of teeth, and thus an improved understanding of such heterogeneous character is desired (Bertassoni et al., 2012). The elastic response between the hybrid layer and the bottom of the hybrid layer has been scarcely compared, much less in the caries-affected dentin substrate. Scanning probe microscopes and, in particular, the atomic force microscope have facilitated the imaging and analysis of biological surfaces with little or no sample preparations (Habelitz et al., 2002). Dentin is a composite of collagen molecules and nanocrystals of hydroxyapatite. Akin to bone (Fratzl et al., 2004), it derives its mechanical behavior from the collective

contributions of these elements and their structural arrangements over length scales ranging from the nano- to the microscale (Kinney et al., 2005). Nanoindentation is the most commonly applied means of testing the mechanical properties of materials or substrates (Poon et al., 2008).

The vast majority of the research work has been focused on the histological, microscopic and mechanical aspects of carious dentin, but rarely on the underlying molecular structure which is integral to a full understanding of the disease, especially its effect on the mineral content and collagen matrix (Liu et al., 2014). In this respect, Raman is a powerful tool in generating direct information about the molecules of a sample. Thereby, this study was complemented with Raman spectroscopy and cluster analysis, that offers nondestructive measures and provide an insight on biochemical nature and molecular structure, and emission spectroscopies of tissue. It is used as a quantitative chemical assessment methodology for biological samples in conjunction with the fact that the Raman peak intensity is proportional to the number of molecules within the volume of the scanned area (Milly et al., 2014). It is a non-destructive and sensitive method capable of identifying individual spectral bands arising from the inorganic calcium phosphate crystals and the protein/lipid constituents of dentin (Wang et al., 2009). Raman mapping, in combination with multivariate data analysis, is a label free imaging method for the analysis of dentin sections. This combined approach yields images depicting a semi-quantitative distribution of the biochemical species in the tissue with high resolution (Bonifacio et al., 2010). Micro-Raman mapping technique appeared to offer a powerful method to directly analyze the resin-dentin interface's constituents and their distribution after placing the restoration and further application of mechanical stimuli. Various methods of multivariate analysis (Almahdy et al., 2012; Toledano et al., 2014b), like principal component analysis (PCA), hierarchical cluster

analysis (HCA) and clustering k-means (KMC) have been established for analyzing two dimensional *data*. Compared to the conventional histological and microscopic methods Raman spectroscopy and cluster analysis result advantageous because they are fast, non-intrusive, stain-free, quantitative and less prone to human subjectivity. The combination of various chemometric methods is essential in providing different images conveying complementary information about the tissue, for studying biochemical and morphological changes during resin-dentin interface degradation and remineralization. The innovative Zn-doped light-curable materials to be tested in this study might be able to induce a therapeutic remineralizing effect on the partially demineralized resin-carious dentin interface.

This investigation assessed the chemical interaction and mechanical performance of caries-affected dentin surfaces treated with Zn-doped etch-and-rinse adhesives. The purpose of this study was to evaluate the ability of etch-and-rinse zinc-doped adhesives to induce functional remineralization at the bonded dentin interface created by using two different demineralization procedures of the caries-affected dentin surface, and after *in vitro* mechanical loading application. This study tested the null hypotheses that functional remineralization of the resin-caries affected dentin interface obtained with zinc-doped adhesives is not produced neither influenced by different etching procedures, after load cycling.

2. MATERIAL AND METHODS

2.1. Specimen preparation, bonding procedures and mechanical loading

Thirty six human third molars with occlusal caries were obtained with informed consent from donors (20–40 year of age), under a protocol approved by the Institution Review Board (891/2014). Molars were stored at 4ºC in 0.5% chloramine T for up to 1

month before use. A flat mid-coronal carious dentin surface was exposed using a hard tissue microtome (Accutom-50; Struers, Copenhagem, Denmark) equipped with a slow-speed, water-cooled diamond wafering saw (330-CA RS-70300, Struers, Copenhagen, Denmark). The inclusion criteria for carious teeth were that the caries lesion, surrounded by sound dentin, should be limited to the occlusal surface, and it is extended at least half the distance from the enamel-dentin junction to the pulp chamber. To obtain caries-affected dentin, grinding was performed by using the combined criteria of visual examination, surface hardness using a dental explorer, and staining by a caries detector solution (CDS, Kuraray Co., Ltd., Osaka, Japan). Using this procedure it was removed all soft, stainable, carious dentin. It was left the relatively hard, caries-affected light pink staining dentin, on the experimental side (Erhardt et al., 2008). A 180-grit silicon carbide (SiC) abrasive paper mounted on a water-cooled polishing machine (LaboPol-4, Struers, Copenhagem, Denmark) was used to produce a clinically relevant smear layer (Koibuchi et al., 2001).

An etch-and-rinse adhesive system, Single Bond Plus (3M ESPE, St Paul, MN, USA) (SB), was tested. It was zinc doped by mixing the bonding resin with 20 wt% ZnO microparticles (Panreac Química, Barcelona, Spain) (SB-ZnO) or with 2 wt% $ZnCl_2$ (Sigma Aldrich, St Louis, MO, USA) (SB-$ZnCl_2$). To achieve complete dissolution of $ZnCl_2$ and dispersion of ZnO nanoparticles, adhesive mixtures were vigorously shaken for 1 min in a tube agitator (Vortex Wizard, Ref. 51075; Velp Scientifica, Milan, Italy). The complete process was performed in the dark. Employed chemicals and adhesives description are provided in Table 1.

Table 1. Materials and chemicals used in this study and respective manufacturers, basic formulation and mode of application.

Product details	**Basic formulation**	**Mode of application**
Adper Single Bond Plus (SB) (3M ESPE, St Paul, MN, USA)	Bis-GMA HEMA dimethacrylates ethanol water a novel photoinitiator system a methacrylate functional copolymer of polyacrylic polyitaconic acids	**Dentin conditioning** 37% H_3PO_4 (15 s) 0.5 M EDTA (60 s) **Adhesive application** -Rinse with water - Adhesive application (30 s) - Light activation (15 s)
Zinc oxide (Panreac Química SA, Barcelona, Spain).		
Zinc chloride 2-hydrate powder (Sigma Aldrich, St. Louis, MO, USA).		
Phosphoric acid 37% (Braun Medical SA, Barcelona, Spain).		
EDTA (Sigma Aldrich, St. Louis, MO, USA).		
X-Flow^{TM} (Dentsply, Caulk, UK)	Strontium alumino sodium fluoro-phosphorsilicate glass, di- and multifunctional acrylate and methacrylate resins, DGDMA, highly dispersed silicon dioxide UV stabilizer,ethyl-4-dimethylamino-benzoate camphorquinone, BHT, iron pigments, titanium dioxide	
SBF (pH=7.45)	NaCl 8.035 g (Sigma Aldrich, St. Louis, MO, USA). $NaHCO_3$ 0.355 g (Sigma Aldrich, St. Louis, MO, USA). KCl 0.225 g (Panreac Química SA, Barcelona, Spain) $K_2HPO_4 \cdot 3H_2O$ 0.231 g (Sigma Aldrich, St. Louis, MO, USA). $MgCl_2 \cdot 6H_2O$ 0.311 g (Sigma Aldrich, St. Louis, MO, USA). 1.0 M – HCl 39 ml (Sigma Aldrich, St. Louis, MO, USA) $CaCl_2$ 0.292 g (Panreac Química SA, Barcelona, Spain) Na_2SO_4 0.072 g (Panreac Química SA, Barcelona, Spain) Tris 6.118 g (Sigma Aldrich, St. Louis, MO, USA). 1.0 M – HCl 0–5 ml (Panreac Química SA, Barcelona, Spain)	

Abbreviations: Bis-GMA: bisphenol A diglycidyl methacrylate; HEMA: 2-hydroxyethyl methacrylate; EDTA: ethylenediaminetetraacetic acid; DGDMA: diethyleneglycol dimethacrylate phosphate; BHT: butylated hydroxytoluene; SBF: simulated body fluid solution; NaCl: sodium chloride; $NaHCO_3$: sodium bicarbonate; KCl: potassium chloride; $K_2HPO_4 \cdot 3H_2O$: potassium phosphate dibasic trihydrate; $MgCl_2 \cdot 6H_2O$: magnesium chloride hexahydrate; HCl: hydrogen chloride; $CaCl_2$: Calcium chloride; Na_2SO_4: sodium sulfate; Tris: tris(hydroxylmethyl) aminomethane.

The specimens were divided into the following groups (n=6) based on the tested adhesive systems and dentin-etching procedure: (i) SB was applied on 37% phosphoric acid (PA) treated dentin, 15 s (PA + SB); (ii) SB was applied on EDTA-treated dentin, 0.5 M, 60 s (EDTA + SB); (iii) SB-ZnO was applied on 37% PA treated dentin; (iv) SB-ZnO was applied on EDTA-treated dentin, 0.5 M, 60 s; (v) SB-$ZnCl_2$ applied on 37% PA; (vi) SB-$ZnCl_2$ applied on EDTA-treated dentin, 0.5 M, 60 s.

The bonding procedures were performed in moist caries-affected dentin following the manufacturer´s instructions. A flowable resin composite (X-Flow™, Dentsply, Caulk, UK) was placed incrementally in five 1 mm layers and light-cured with a Translux EC halogen unit (Kulzer GmbH, Bereich Dental, Wehrheim, Germany) for 40 s. Half of the carious teeth were stored for 24 h in simulated body fluid solution (SBF) (ISO 23317 method), and the other half were submitted to mechanical loading, in SBF (100,000 cycles, 3 Hz, 49 N) (S-MMT-250NB; Shimadzu, Tokyo, Japan) (Toledano et al., 2014b). The load cycling lasted for 9 hours and 15 minutes; the rest of the time until complete 24 h, the loaded specimens were kept in SBF, at 37 ºC.

2.2. AFM nano-indentation

An atomic force microscope (AFM-Nanoscope V, Digital Instruments, Veeco Metrology group, Santa Barbara, CA, USA) equipped with a Triboscope indentor system (Hysitron Inc., Minneapolis, MN, USA) and a Berkovich indenter (tip radius 20 nm) was employed in this study. For each subgroup, three slabs were tested. On each slab, five indentation lines were executed in five different mesio-distal positions along the interface in a straight line, starting from the hybrid layer down to the bottom of the hybrid layer. Indentations were performed with a load of 4000 nN and a time function of 10 s. The indenter was progressively (at a constant rate) pressed over the sample up

to a peak load of 4000 μN (loading part of the experiment) and, afterwards, the load was progressively released to zero value (unloading part of the experiment). Specimens were scanned in a hydrated condition. To avoid dehydration a layer of ethylene glycol over the specimen surface was applied, preventing water evaporation during a typical 25-to-30-min scanning period (Ryou et al., 2011). The distance between each indentation was kept constant by adjusting the distance intervals in 5 (±1) μm steps (Toledano et al., 2013). Hardness (*Hi*) and modulus of elasticity (*Ei*) data were registered in GPa.

At this point, it is recommended to mention that the nanoindentation modulus obtained by this method was usually referred to as Young's modulus in the literature, which however should not be confounded with the Young's modulus obtained at the macroscopic level by traction/compression experiments. Nevertheless, it has been kept Young's modulus terminology for the nanoindentation modulus along this manuscript, as it is the usual case in most of the literature.

The load, F, was obtained as a function of the penetration depth, h, of the indenter in the sample. From the slope of these load-*vs*.-depth curves the nanoindentation modulus (Young's modulus) could be obtained by application of different theoretical models (Han et al., 2011; Oliver and Pharr, 1992). One of these is the Oliver-Pharr method, which is based on a continuum, isotropic, homogeneous elastic contact model to determine the reduced modulus, E_r. In this model the slope, S, of the unloading portion of the load-*vs*.-depth data is used to obtain E_r according to the following equation (Oliver and Pharr, 1992):

$$S = \frac{dF}{dh} = \frac{2}{\sqrt{\pi}} E_r \sqrt{A}, \qquad (1)$$

where A is the projected contact area of the hardness impression of the indenter. Then, E_i of the sample is obtained through the following expression:

$$\frac{1}{E_r} = \frac{\left(1-\nu_{ind}^2\right)}{E_{ind}} + \frac{\left(1-\nu_i^2\right)}{E_i}, \qquad (2)$$

In this expression "*i*" subscript refers to the tested sample and "*ind*" subscript to the indenter. ν and *E* are the Poisson's ratio and the Young's modulus, respectively. For hard materials, as dentin, usually, $E_{ind} >> E_i$ and, thus, the contribution of the indenter in equation (2) can be neglected. With regard to the nanohardness of the sample, *H*, it is defined as:

$$H = \frac{F_{\max}}{A}, \qquad (3)$$

Where F_{max} is the peak load. In this work, values of nanohardness and Young's modulus were automatically calculated by using the software Triboscan Quasi version 8.4.2.0 (Hysitron, Inc).

Data were analyzed by two-way ANOVA (independent factors were mechanical loading and adhesive procedure) and Student–Newman–Keuls multiple comparisons ($P < 0.05$).

2.3. Raman spectroscopy and cluster analysis.

A dispersive Raman spectrometer/microscope (Horiba Scientific Xplora, Villeneuve d´Ascq, France) was also used to analyze bonded interfaces. A 785-nm diode laser through a X100/0.90 NA air objective was employed. Raman signal was acquired using a 600-lines/mm grafting centered between 900 and 1,800 cm^{-1}. Chemical mapping of the interfaces were performed. For each specimen two areas 25μm x 25μm area of the interfaces at different sites were mapped using 2 μm spacing at X axis and 1 μm at Y axis. Chemical mapping was submitted to K-means cluster (KMC) analysis

using the multivariate analysis tool (ISys® Horiba), which includes statistical pattern to derive the independent clusters. However, Ward's method was employed to get some sense of the number of clusters and the way they merge from the dendrogram. The aim of a factor analysis lies in the effective reduction of the dataset dimension while maintaining a maximum of information. This method was used to model the data and to determine spectral variances associated for data differentiation. It resulted in the calculation of a new coordinate system whereby variations of the dataset is described via new axes, principal components (PCs). The K-means clustering is a method of analysis based on a centroid model which aims to partition *n* observations into *k* clusters in which each observation belongs to the cluster with the nearest mean (Almahdy et al., 2012). The natural groups of components (or *data*) based on some similarity and the centroids of a group of *data* sets were found by the clustering algorithm once calculated by the software. To determine cluster membership, this algorithm evaluated the distance between a point and the cluster centroids. The output from a clustering algorithm was basically a statistical description of the cluster centroids with the number of components in each cluster. The biochemical content of each cluster was analyzed using the average cluster spectra. Four clusters were identified and values for each cluster such as adhesive, hybrid layer, bottom of hybrid layer and dentin, within the interface, were independently obtained. Principal component analysis (PCA) decomposed *data* set into a bilinear model of linear independent variables, the so-called principal components (PC_S). Two principal components were selected for the present study at interfaces: hybrid layer (HL) and bottom of hybrid layer (BHL). The observed spectra were described at 900-1800 cm^{-1} with 10 complete overlapping Gaussian lines, suggesting homogeneous data for further calculations (Ager et al., 2005).

As the cluster centroids are essentially means of the cluster score for the elements of cluster, the mineral and organic components of dentin hybrid layers were examined for each cluster. A comparison of the spectra that were collected from the two specimens which compose each subgroup indicated complete overlap, suggesting similarity between both measurements. It was hence used for identifying significant spectral differences among distinct substrata. For hierarchical cluster analysis (HCA) Raman imaging, each dataset was assessed to automatically distinguish regions of the scanned area with different Raman features (Vanna et al., 2015). For each specimen, a 12μm x 12μm area of the surface was mapped using 1 μm spacing at X and Y axes, at 100x magnification. A total of 144 points were performed per map. In the cluster analysis routine, PCA scores were taken as input variables, squared Euclidean distances were used as distances measures, and Ward's algorithm was used to partition Raman spectra into cluster. Clusters were created following Ward's technique (HCA) and the dendrogram was calculated applying three factor spectra or principal components, corresponding with three different components at the resin-dentin interface (red, dentin; green hybrid layer; blue, adhesive). The number of clusters, three, were chosen according to several issues, such as the dendrogram structure, the false-color maps and the cluster centroid (Bonifacio et al, 2010). These three levels of HCA clustering were used in order to obtain HCA Raman images with a good description of the dentin composition. Each cluster was assigned to a different color, thus obtaining a false color-image of the substrate on the basis of similar spectral features. Once clusters were formed (HCA images), average spectra (centroids) (HCA results) were calculated for each cluster. For each point of analysis, all spectra described for each cluster were averaged to obtain the mean cluster spectrum. Each mean cluster spectrum was then corrected by subtracting the mean spectrum of the background measured around the

specific location of analysis. The aim of a factor analysis lies in the effective reduction of the dataset dimension while maintaining a maximum of information. This method was used to model the data and to determine spectral variances associated for data differentiation. It resulted in the calculation of a new coordinate system whereby variations of the dataset is described via new axes, principal components (PCs). At this point, the mineral component of dentin was assessed as follows:

Relative presence of mineral:

1. *Phosphate* (960 cm^{-1}) *and carbonate* (1070 cm^{-1}) *peaks and areas of their bands*. Peak heights were processed in absorbance units.
2. *Relative mineral concentration* (RMC) (i.e., mineral-to-matrix ratio): It was inferred from the visible ratio of the intensities of the peaks at 960 cm^{-1} (phosphate) (PO_4^{3-}) and 1003 cm^{-1} (phenyl group), the aromatic ring of phenylalanine residues in collagen. These indexes concerned with the maximum relative degree of mineralization (Karan et al., 2009; Schwartz et al., 2012).

Crystallinity:

It was evaluated based on the full width at half maximum (FWHM) of the phosphate band at 960 cm-1 and carbonate band at 1070 cm^{-1}. These indexes expressed the crystallographic or relative atomic order, since narrower peaks suggest less structural variation in bond distances and angles (Schwartz et al., 2012). In general, the narrower the spectral peak width is, the higher the degree of mineral crystallinity (Karan et al., 2009).

Gradient in mineral content (GMC), or carbonate content of the mineral crystallites: It was assessed as the relationship between the ratio of heights at 1070 cm^{-1} (carbonate) (CO_3^{2-}) to 960 cm-1 (phosphate) (PO_4^{3-}), indicating carbonate substitution for phosphate (Schwartz et al., 2012).

Modified phosphate peaks ratio (mPPR): it assesses the ratio between the mineral peak at 960 cm^{-1} (phosphate) (PO_4^{3-}), within the demineralized zone and the mineral peak (PO_4^{3-}) within the caries-affected dentin (Milly et al., 2014).

The organic component of dentin was analyzed examining the following parameters:

Normalization: Phenyl group: The peak at 1003 cm^{-1}, which is assigned to C-C bond in the phenyl group, was used for normalization (Xu and Wang, 2011).

Crosslinking:

1. Pyridinium ring vibration: In the spectra, the peak appeared at 1030/1032.7 cm-1, is assigned to the C-C in pyridinium ring vibration which has a trivalent amino acid crosslinking residue (Daood et al., 2013). The relative intensity of this peak increases after the crosslinking formation (Jastrzebska et al., 2003).
2. Ratio pyridinium/phenyl (1032/1003 cm^{-1}): the higher the ratio, the greater the extend of collagen cross-linking (Jastrzebska et al., 2003; Xu and Wang, 2012).
3. Ratio 1660 (amide I)/1690-1701cm^{-1}: It is a collagen quality parameter (Salehi et al., 2013), and decreases when mineralization increases.
4. Ratio 1003 (phenyl)/1450 (CH_2) cm^{-1}: It arises preceding deposition of HAP (hydroxyapatite) crystals within the structure (Wang et al., 2009).
5. AGEs (advance glycation end products)-pentosidine at 1550 cm^{-1}, interpreted as a marker of the aging process (Sell and Monnir, 1989).

Nature of collagen:

1. Amide III, CH_2 and amide I: The peaks at 1246/1270, 1450 and 1655/1667 cm^{-1}, assigned to amide III, CH_2 and amide I, respectively, are sensitive to the molecular conformation of the polypeptide chains (Jastrzebska et al., 2003; Xu and Wang, 2011). The decrease of amide I peak indicates damage or removal of

collagen fibrils (Xu and Wang, 2012). 1450 cm^{-1} (CH deformation bands) is generally assigned to proteins, lipids and carbohydrates; it is in accordance with the immature stage (Vanna et al, 2015).

2. Amide II peak, at 1510 cm^{-1} (Ager et al., 2005), determines the secondary structure content of proteins, underlying the distinction between ordered and disordered helices (Dousseau and Pézolet, 1990)
3. Ratio amide I/amide III concerned the organization of collagen.
4. Ratio amide III /CH2 wagging mode indicates the structural differences (Salehi et al., 2013).
5. Ratio amide I/CH_2 indicates altered collagen quality (Salehi et al., 2013).
6. Ratios amide III and I/AGEs-Pentosidine, indicatives of the glycation reaction vs collagen scaffolding (Salehi et al., 2013).
7. 1340 cm^{-1}peak: This signal has been assigned to protein α-helices where intensity is sensitive to molecular orientation (Wang et al., 2009).

Degree of adhesive efficacy:

1. *Degree of conversion of adhesive*

   Ratio 1637/1608. The peak appearing at 1637 cm-1 is associated with C=C of methacrylate, and the peak at 1608 cm-1 is related to C-C in phenyl of adhesive monomer (Xu and Wang, 2012).

2. *Bis-GMA penetration*

   Ratio1113/1667. The peak appearing at 1113 cm^{-1} is associated with C-O-C of adhesive, and the peak at 1667 cm^{-1} is related to amide I (Wang and Spencer, 2003; Xu and Wang, 2012).

3. *Adhesive (Bis-GMA and HEMA) penetration*

Ratio 1450/1667. The peak appearing at 1450 cm^{-1} is assigned to the CH_2 group of both Bis-GMA and HEMA, and the peak at 1667 cm^{-1} is related to amide I (Wang and Spencer, 2003; Xu and Wang, 2012).

2.4. Light microscopy–Masson's trichrome staining

Thirty six additional human carious third molars were bonded and prepared as explained above and used for the histo-morphological evaluations. The medial aspects of each resin–dentin bonded slice was fixed in a glass holder with a photo curing adhesive (Technovit 7210 VLC, Heraeus Kulzer GmbH Co., Werheim, Germany) and ground with SiC papers of increasing fine grits (800, 1000, 1200 and 4000) in a polisher (Exakt, Apparatebau D-2000, Norderstedt, Germany) until its thickness was approximately 10 mm. Slices were stained with Masson's trichrome for differentiation of resin and non-resin encapsulation of the exposed collagen. This dye has a high affinity for cationic elements of normally mineralized type I collagen, resulting in staining collagen green, and when demineralized, resulting in different coloration, generally red; collagen coated with adhesive stains orange and pure adhesive appears beige. Slices with adherent stained sections were dehydrated through ascending ethanol and xylene. The sections were cover slipped and examined by light microscopy (BH-2, Olympus, Tokyo, Japan) at 100× magnifications. Three slices were prepared from each specimen, and images were digitalized in a scanner (Agfa Twin 1200, Agfa-Gevaert NV Mortsel, Belgium). In each specimen, the presence or absence of a red band (that would correspond to demineralized dentin) was observed. A qualitative assessment of the collagen encapsulation was completed by observing color differences within the interfacial zones of resin-dentin interfaces (Toledano et al., 2015).

3. RESULTS AND DISCUSSION

Attained nanohardness and Young's modulus at the hybrid layer and at the bottom of hybrid layer are shown in Figures 1 and 2, respectively. The 3D micro-Raman maps and the Raman spectra of principal components are displayed in Figure 3. Light micrographs of caries-affected dentin treated with phosphoric acid or EDTA are provided in Figures 4 and 5, respectively. Hierarchical cluster analysis images and results are included in Figures 6 and 7, respectively. Tables 2, 3 and 4 show the Raman chemical analysis of the mineral, organic and adhesive components, at the resin-dentin interface.

Figure 1

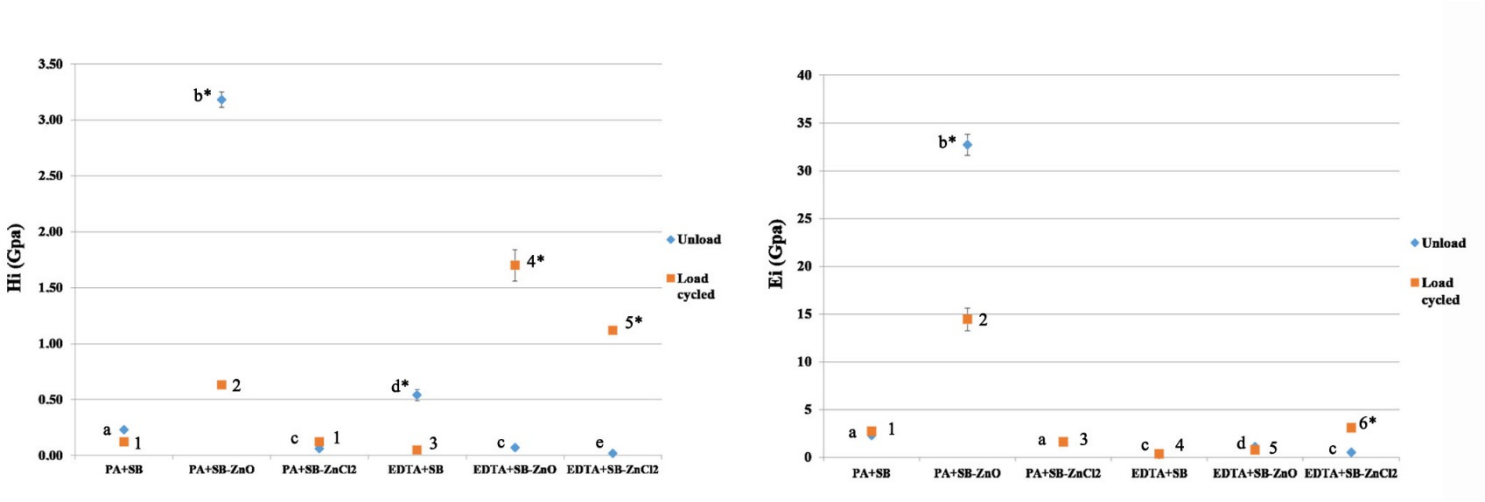

Figure 1: Mean and SD of nanohardness (*Hi*) and Young's modulus (*Ei*) (GPa) measured at the experimental hybrid layers (HL) in caries-affected dentin. PA: Phosphoric acid, SB: Single Bond, EDTA: ethylenediaminetetraacetic acid. Identical letters indicate no significant differences between unloaded restorations. Identical numbers indicate no significant differences between load cycled restorations. * indicates significant differences between unloaded and load cycled restorations within the same experimental adhesive group.

Figure 2

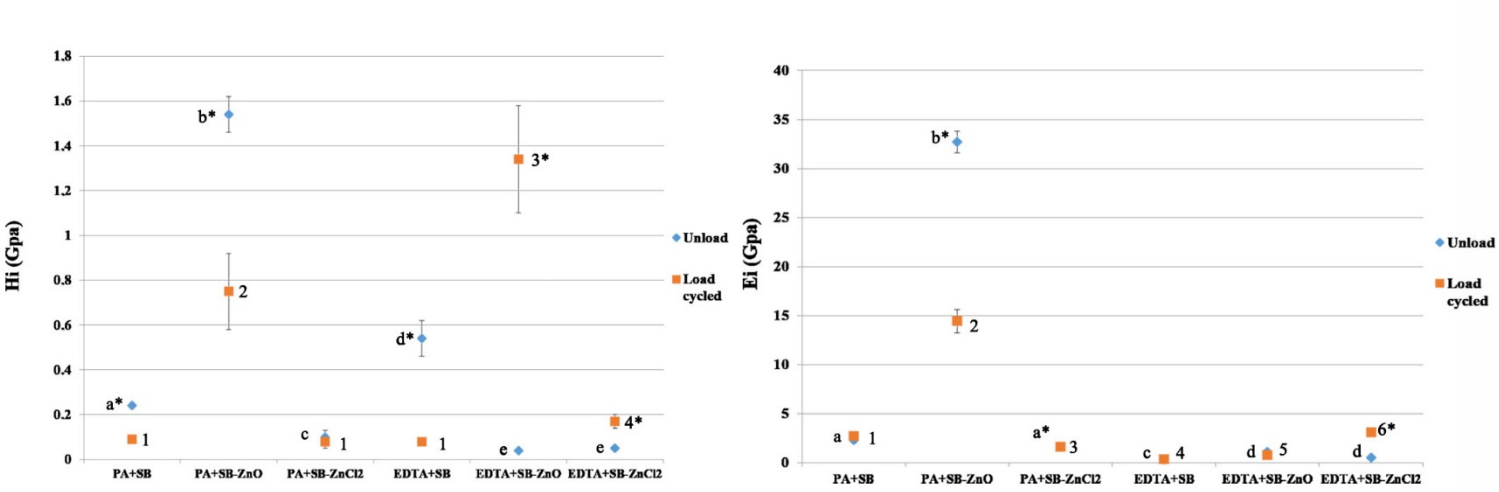

Figure 2: Mean and SD of nanohardness (*Hi*) and Young's modulus (*Ei*) (GPa) measured at the experimental bottom of hybrid layer (BHL) in caries-affected dentin. PA: Phosphoric acid, SB: Single Bond, EDTA: ethylenediaminetetraacetic acid. Identical letters indicate no significant differences between unloaded restorations. Identical numbers indicate no significant differences between load cycled restorations.

* indicates significant differences between unloaded and load cycled restorations within the same experimental adhesive group.

Figure 3.1.

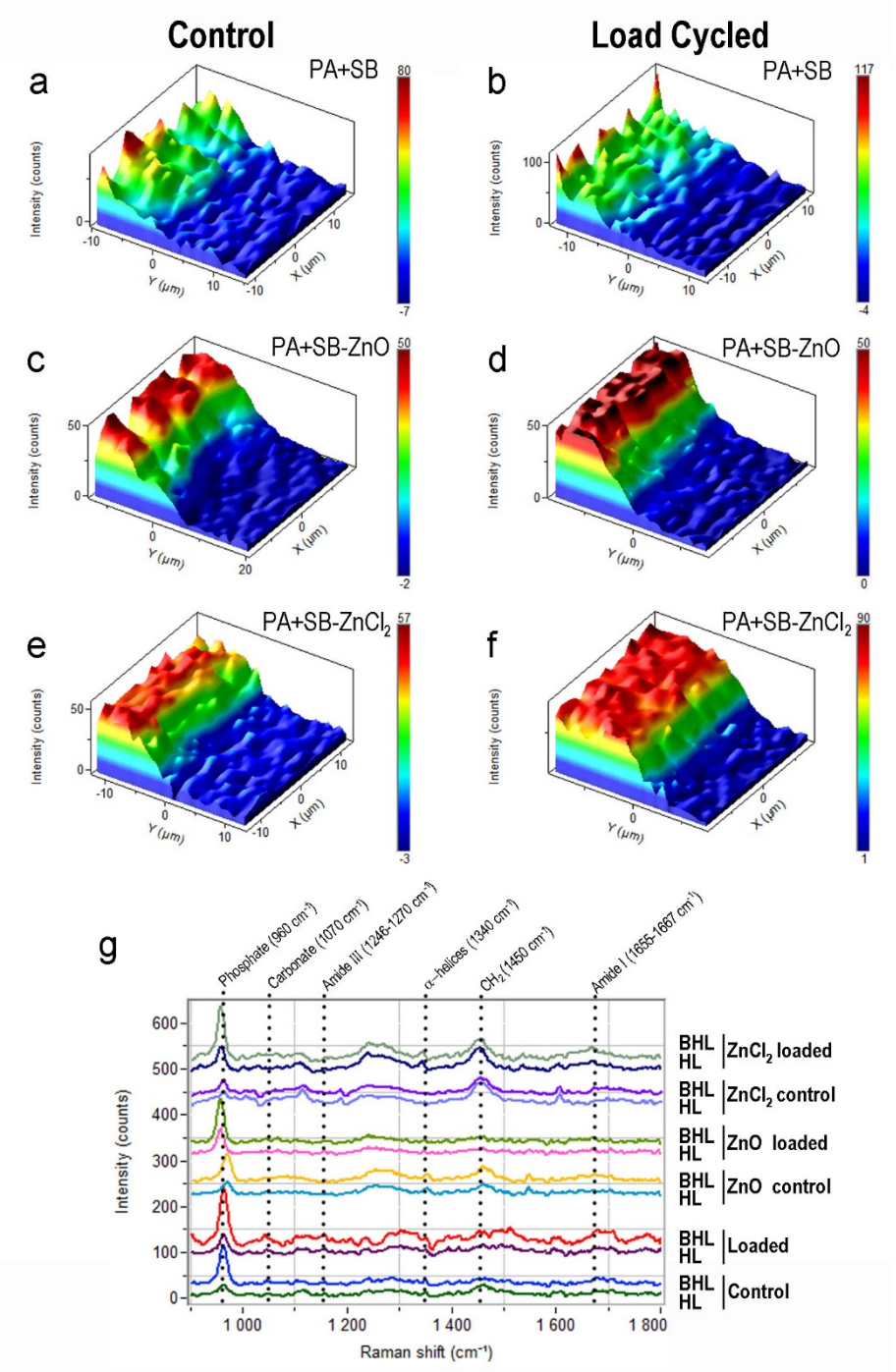
Control
Load Cycled
a
PA+SB
b
PA+SB
c
PA+SB-ZnO
d
PA+SB-ZnO
e
PA+SB-ZnCl2
f
PA+SB-ZnCl2
Intensity (counts)
Y (µm)
X (µm)
g
Phosphate (960 cm-1)
Carbonate (1070 cm-1)
Amide III (1246-1270 cm-1)
α-helices (1340 cm-1)
CH2 (1450 cm-1)
Amide I (1655-1667 cm-1)
Intensity (counts)
Raman shift (cm-1)
BHL
HL
ZnCl2 loaded
ZnCl2 control
ZnO loaded
ZnO control
Loaded
Control

Figure 3.2.

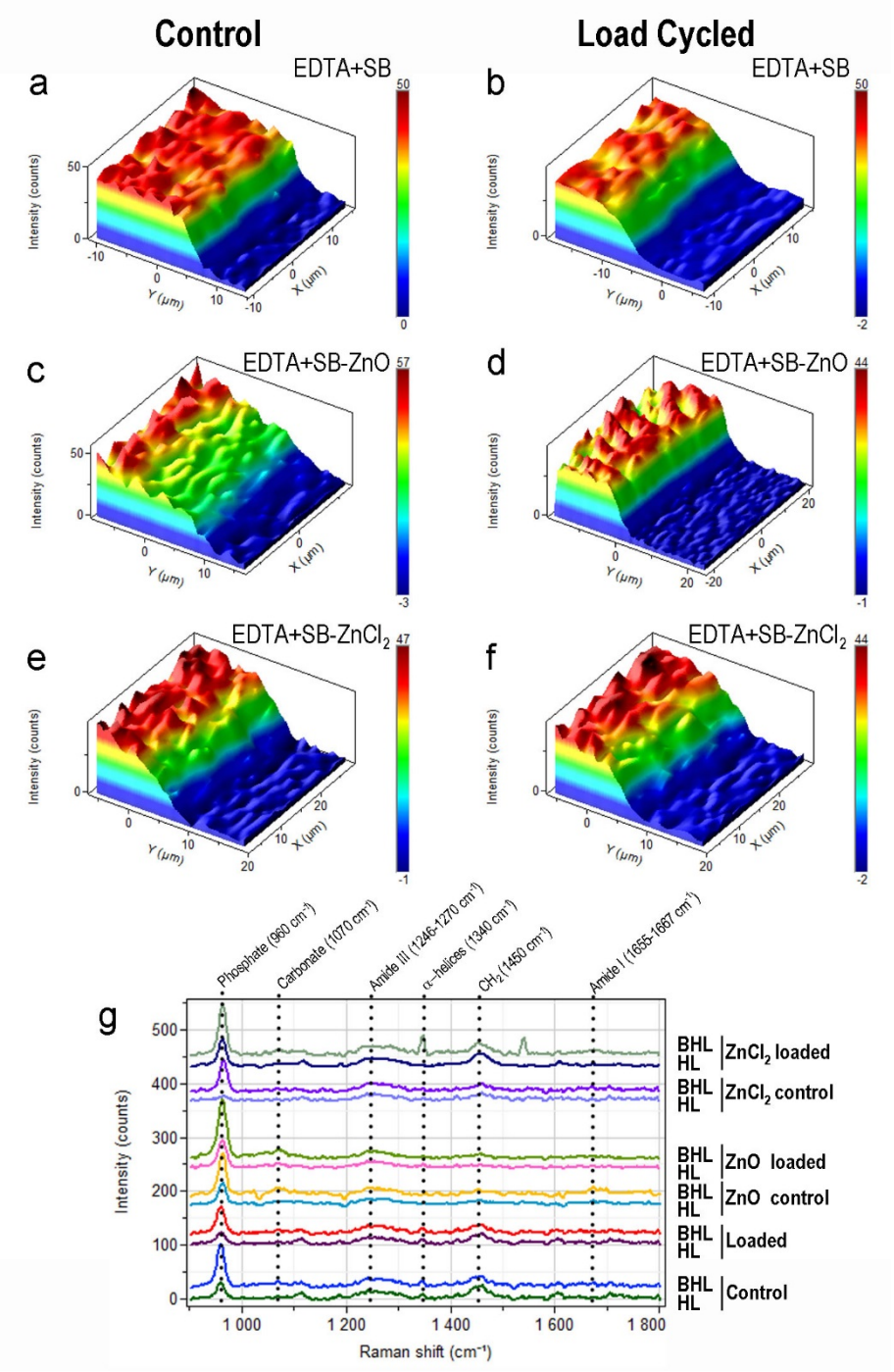

Figure 3. 1, 3D micro-Raman map of the phosphate peak (961 cm^{-1}) intensities at the caries-affected dentin bonded interface of phosphoric acid (PA)-treated dentin surfaces plus Single Bond (SB) adhesive application (PA+SB). [In the color scheme shown

(from Fig “a” to “f”), the redder color corresponds with higher values of the locally measured phosphate peak (961 cm^{-1}) intensities]: unloaded (left), or load cycled (right). (a, b) Non-doped; (c, d) SB-ZnO doped; (e, f) SB-$ZnCl_2$ doped. (g) Raman *spectra*of principal components (PCs): HL, hybrid layer; BHL, bottom of hybrid layer for each PA+SB group. **2**, 3D micro-Raman map of the phosphate peak (961 cm^{-1}) intensities at the caries-affected dentin bonded interface of EDTA-treated dentin surfaces plus Single Bond (SB) adhesive application (EDTA+SB). [In the color scheme shown (from Fig “a” to “f”), the redder color corresponds with higher values of the locally measured phosphate peak (961 cm^{-1}) intensities]: unloaded (left), or load cycled (right). (a, b) Non-doped; (c, d) SB-ZnO doped; (e, f) SB-$ZnCl_2$ doped. (g) Raman *spectra* of principal components (PCs): HL, hybrid layer; BHL, bottom of hybrid layer for each EDTA+SB group.

Figure 4

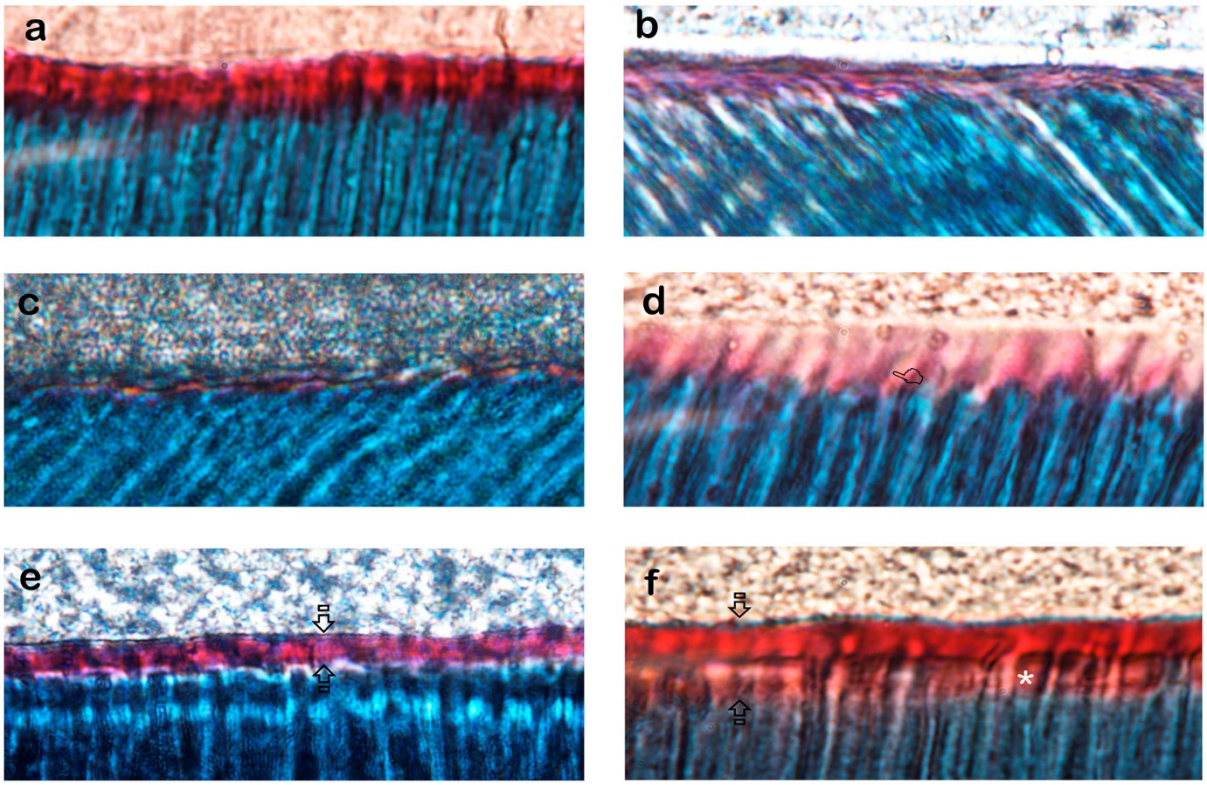

Figure 4. Representative light micrographs of PA+SB in CAD specimens; interfaces stained with Masson's trichrome: mineralized dentin stained green, adhesive stained beige, and exposed protein stained red. Original magnification: 150X (a) PA+SB control (unloaded). (b) PA+SB loaded. (c) PA+SB-ZnO. (d) PA+SB-ZnO load cycled. (e) PA+SB-$ZnCl_2$. (f) PA+SB-$ZnCl_2$ load cycled. Intense (a, b, e, f) or faint (c, d) evidence of partial demineralization and/or exposed protein (red stain) is detectable at the resin/dentin interface. New tubular dentin walls formation are detected, in PA+SB-ZnO, reproducing the sinusoidal primary curvatures (pointer) (d). Both PA+SB-$ZnCl_2$ doped groups showed an increment in red intensity (e) and width (f), revealing a noticeable presence of uncovered decalcified dentin (arrows) at the interface, permitting to observe the scarce remineralization of the partially-demineralized dentin layer

(asterisk). PA, phosphoric acid; SB, single bond; CAD: caries-affected dentin; ZnO, zinc oxide; $ZnCl_2$, zinc chloride.

Figure 5

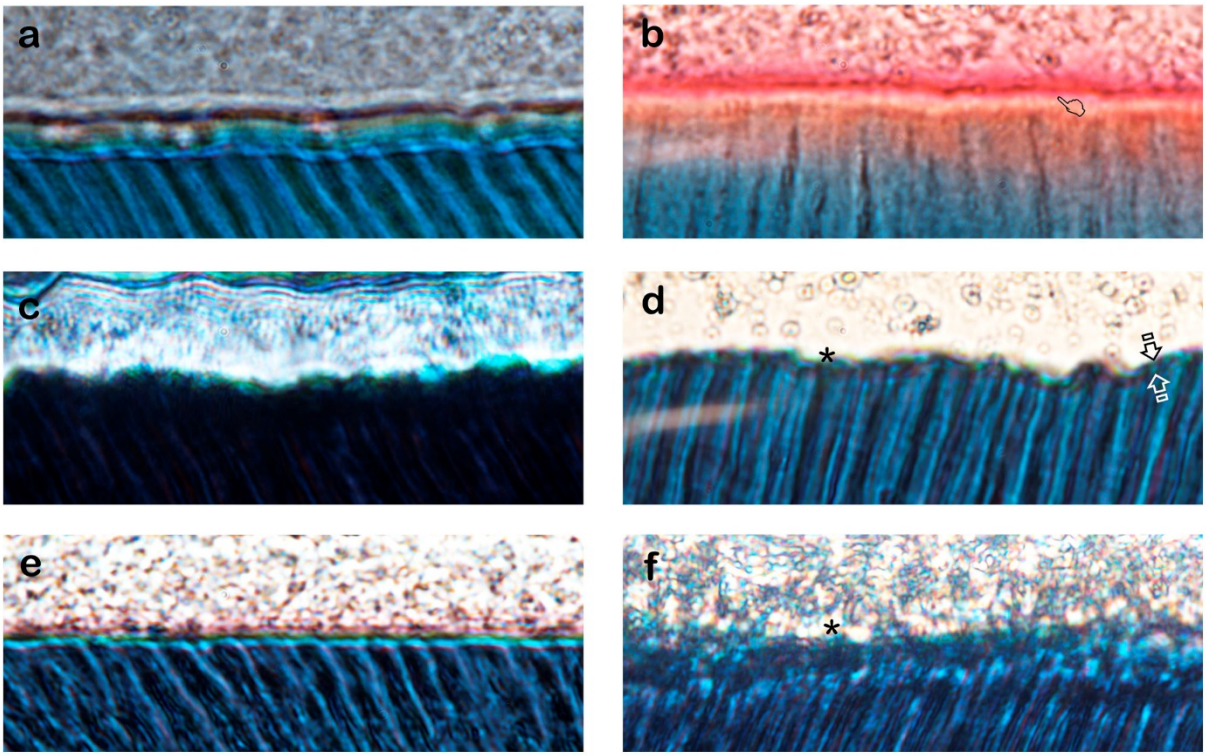

Figure 5. Representative light micrographs of EDTA+SB in CAD specimens; interface stained with Masson's trichrome: mineralized dentin stained green, adhesive stained beige, and exposed protein stained red. Original magnification: 150X (a) EDTA+SB control (unloaded). (b) EDTA+SB loaded. (c) EDTA+SB-ZnO. (d) EDTA+SB-ZnO load cycled. (e) EDTA+SB-$ZnCl_2$. (f) EDTA+SB-$ZnCl_2$ load cycled. Absence of unprotected collagen layers were detected in the majority of specimens (c, d, e, f). Less exposed proteins were observed at both the resin dentin interface and tubular area, except in the control group (EDTA+SB) loaded (b) (pointer). Any signs (f) of demineralization and/or exposed protein (red stain) are detectable at the resin/dentin interface of Zn-doped and loaded samples (d, f) (asterisk); the thinnest (arrows) uncovered decalcified dentin was observed in EDTA+SB-ZnO load cycled (d). EDTA,

ethylendiaminetetraacetic; SB, single bond; CAD: caries-affected dentin; ZnO, zinc oxide; $ZnCl_2$, zinc chloride.

Figure 6

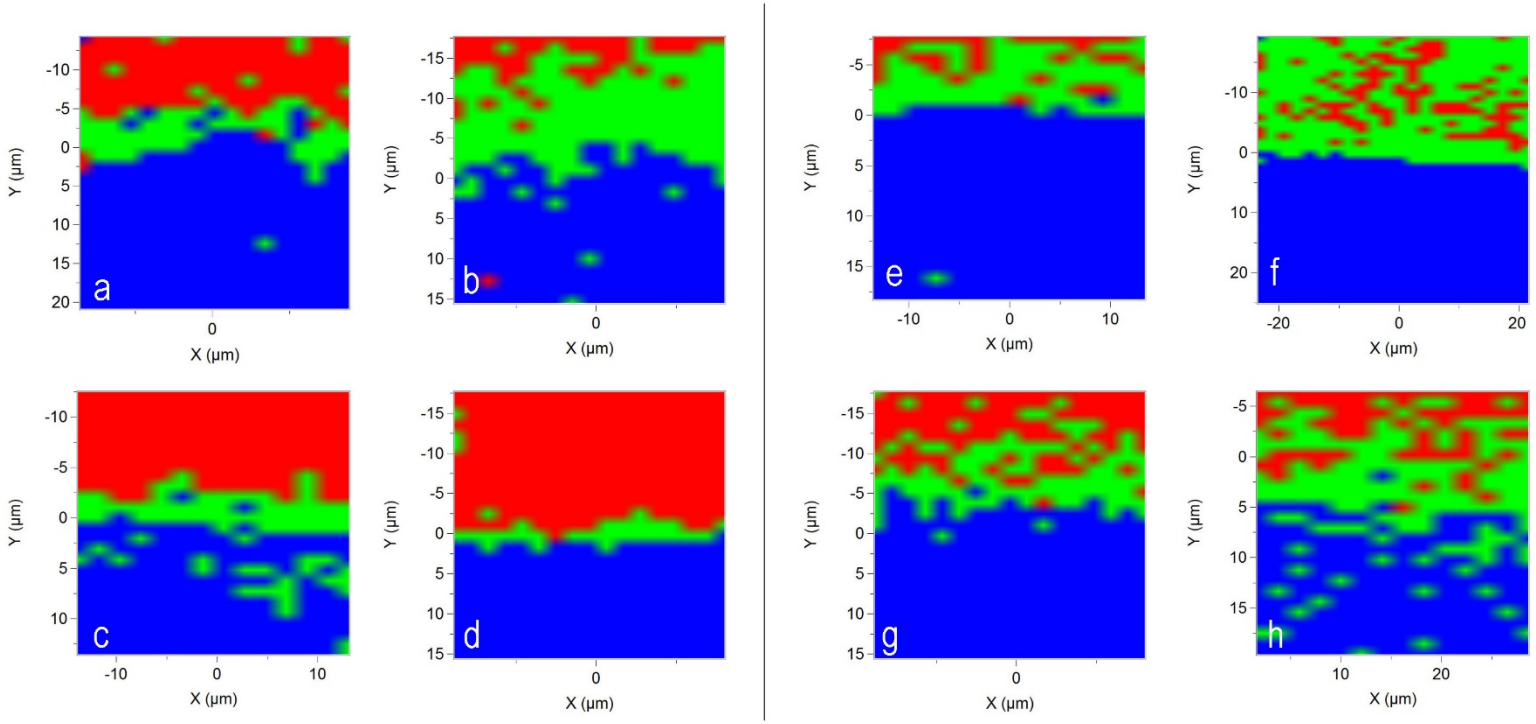

Figure 6. Color mapping from hierarchical cluster analysis **(**HCA) images corresponding to caries-affected dentin bonded interfaces of phosphoric acid (PA) and EDTA-treated dentin plus Single Bond (SB) adhesive application. Three levels of HCA clustering are shown. Areas of distinct colors have differences in Raman spectral distribution and chemical composition. Each cluster is assigned to a different color (red, dentin; green, hybrid layer; blue, adhesive), thus obtaining a false color-image of the substrate on the basis of similar spectral features. (a)

PA+SB-ZnO. (b) PA+SB-ZnO load cycled. (c) PA+SB-$ZnCl_2$. (d) PA+SB-$ZnCl_2$ load cycled. (e) EDTA+SB-ZnO. (f) EDTA+SB-ZnO load cycled. (g) EDTA+SB-$ZnCl_2$. (h) EDTA+SB-$ZnCl_2$ load cycled.

Figure 7

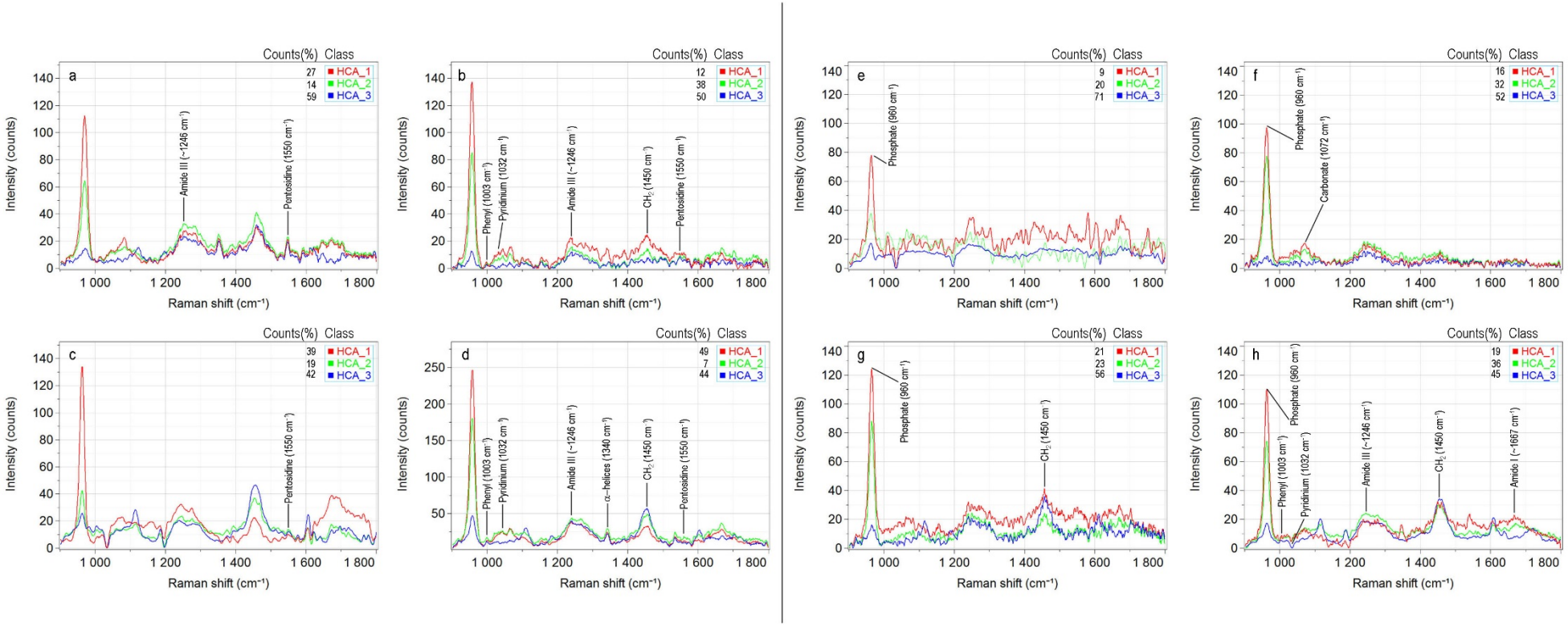

Figure 7. Spectra from hierarchical cluster analysis (HCA) results of caries-affected dentin bonded interface of phosphoric acid (PA) and EDTA-treated dentin surfaces plus Single Bond (SB) adhesive application. (a) PA+SB-ZnO. (b) PA+SB-ZnO load cycled. (c) PA+SB-$ZnCl_2$. (d)

PA+SB-$ZnCl_2$ load cycled. (e) EDTA+SB-ZnO. (f) EDTA+SB-ZnO load cycled. (g) EDTA+SB-$ZnCl_2$. (h) EDTA+SB-$ZnCl_2$ load cycled.

Table 2a. Mineral components in phosphoric acid-treated caries-affected dentin interfaces plus Single Bond adhesive application (PA+SB).

			Relative Presence of Mineral				FWHM	GMC Ratio C/P	mPPR Ratio phosphate peak /caries affected substratum
			Phosphate [961]			Carbonate [1070]			
			Peak	Area	RMC	Peak	Phosphate		
PA + SB	Control	HL	29.93	343.8	3.65	17.47	29.93	0.58	0.23
		BHL	91.74	2265.74	9.52	10.51	19.35	0.11	0.70
	Load cycled	HL	46.57	1334.67	4.20	7.76	22.58	0.17	0.36
		BHL	132.57	3279.38	10.35	14.21	19.38	0.11	1.01
PA + SB-ZnO	Control	HL	28.47	702.16	74.92	5.44	19.27	0.19	0.22
		BHL	61.06	1505.83	62.31	9.04	19.27	0.15	0.47
	Load cycled	HL	56.06	1376.63	9.75	10.33	19.31	0.18	0.43
		BHL	100.11	2064.06	24.48	15.58	16.12	0.16	0.76
PA + SB-$ZnCl_2$	Control	HL	25.84	737.48	1.53	12.07	22.49	0.47	0.20
		BHL	33.22	684.851	3.26	10.85	16.07	0.33	0.25
	Load cycled	HL	54.74	1345.28	5.38	10.66	19.31	0.19	0.42
		BHL	118.84	2448.23	11.43	14.98	16.09	0.13	0.91

Abbreviations: RMC: Relative Mineral Concentration between mineral/Phenyl (1003); FWHM: Full-width half-maximun; GMC: Gradient in Mineral Content; mPPR: modified Phosphate Peaks Ratio. Peaks positions are expressed in cm^{-1}.

Table 2b. Organics components in phosphoric acid-treated caries-affected dentin interfaces plus Single Bond adhesive application (PA+SB).

			Normalization	Crosslinking				Nature of collagen								
			Phenyl [1003]	Pyrid. [1032]	Ratio [1032/1003]	Ratio phenyl/CH_2 [1003/1450]	AGEs-Pentosidine [1550]	A-III [1246-1270]	CH_2 [1450]	A-I [1655-1667]	Ratio Amide I/ Amide III	Ratio Amide III/ CH_2	Ratio Amide I/ CH_2	Ratio Amide III/ AGEs-Pentosidine	Ratio Amide I/ AGEs-Pentosidine	α-helices [1340]
PA + SB	Control	HL	8.19	10.36	1.26	0.27	9.94	14.7	30.4	16.17	1.10	0.48	0.53	1.48	1.63	14.27
		BHL	9.64	8.72	0.90	0.50	10.46	16.33	19.26	20.92	1.28	0.85	1.09	1.56	2.00	16.83
	Load cycled	HL	11.09	14.24	1.28	0.45	16.03	13.29	24.66	18.89	1.42	0.54	0.77	0.83	1.18	15.81
		BHL	12.81	31.05	2.42	0.34	20.84	13.47	37.33	24.72	1.84	0.36	0.66	0.65	1.19	23.44
PA + SB-ZnO	Control	HL	-0.38	2.41	-6.34	-0.02	15.25	20.07	23.97	9.58	0.48	0.84	0.40	1.32	0.63	14.99
		BHL	0.98	4.61	4.70	0.03	15.83	25.22	33.50	15.27	0.61	0.75	0.46	1.59	0.96	16.05
	Load cycled	HL	5.75	7.43	1.29	0.38	10.77	15.40	14.94	12.70	0.82	1.03	0.85	1.43	1.18	8.38
		BHL	4.09	10	2.44	0.22	11.58	13.96	18.97	15.59	1.12	0.74	0.82	1.21	1.35	10.62
PA + SB-$ZnCl_2$	Control	HL	16.89	-4.35	-0.26	0.36	7.42	15.23	46.71	3.61	0.24	0.33	0.08	2.05	0.49	3.36
		BHL	10.20	-5.53	-0.54	0.27	8.21	16.48	37.37	4.88	0.30	0.44	0.13	2.01	0.59	4.70
	Load cycled	HL	10.17	12.39	1.22	0.20	10.9	34.98	51.51	23.74	0.68	0.68	0.46	3.21	2.18	21.40
		BHL	10.40	15.18	1.46	0.22	12.24	36.02	47.67	29.47	0.82	0.76	0.62	2.94	2.41	20.34

Abbreviations: A: Amide; Pyrid: Pyridinium; AGEs: Advanced glycation end products. Peaks positions are expressed in cm^{-1}.

Table 3a. Mineral components in EDTA-treated caries-affected dentin interfaces plus Single Bond adhesive application (EDTA+SB).

			Relative Presence of Mineral				FWHM	GMC Ratio C/P	mPPR Ratio phosphate peak /caries affected substratum
			Phosphate [961]			Carbonate [1070]			
			Peak	Area	RMC	Peak	Phosphate		
EDTA + SB	Control	HL	31.4	648.21	17.64	5.39	16.13	0.17	0.24
		BHL	82.37	1700.68	15.96	10.11	16.13	0.12	0.63
	Load cycled	HL	21.02	517.28	7.25	5.39	19.32	0.26	0.16
		BHL	50.97	1255.7	17.64	7.61	19.35	0.15	0.39
EDTA + SB-ZnO	Control	HL	43.38	894.34	7.87	8.95	16.07	0.21	0.33
		BHL	81.75	1685.35	13.47	16.23	16.07	0.20	0.62
	Load cycled	HL	52.47	1291.83	19.95	8.36	19.29	0.16	0.40
		BHL	111.24	2738.85	16.17	16.92	19.29	0.15	0.85
EDTA + SB- $ZnCl_2$	Control	HL	9.69	314.44	3.92	4.5	25.71	0.46	0.07
		BHL	56.36	1462.07	12.04	7.3	19.29	0.13	0.43
	Load cycled	HL	55.99	1303.8	11.79	8.3	19.29	0.15	0.43
		BHL	97.39	2008.76	28.23	12.88	16.07	0.13	0.74

Abbreviations: RMC: Relative Mineral Concentration between mineral/Phenyl (1003); FWHM: Full-width half-maximun; GMC: Gradient in Mineral Content; mPPR: modified Phosphate Peaks Ratio. Peaks positions are expressed in cm^{-1}.

Table 3b. Organics components in EDTA-treated caries-affected dentin interfaces plus Single Bond adhesive application (EDTA+SB).

			Normalization	Crosslinking				Nature of collagen								
			Phenyl [1003]	Pyrid. [1032]	Ratio [1032/1003]	Ratio phenyl/CH_2 [1003/1450]	AGEs-Pentosidine [1550]	A-III [1246-1270]	CH_2 [1450]	A-I [1655-1667]	Ratio Amide I/ Amide III	Ratio Amide III/ CH_2	Ratio Amide I/ CH_2	Ratio Amide III/ AGEs-Pentosidine	Ratio Amide I/ AGEs-Pentosidine	α-helices [1340]
EDTA + SB	Control	HL	1.78	2.33	1.31	0.07	4.97	15.31	25.87	3.58	0.23	0.59	0.14	3.08	0.72	9.71
		BHL	5.16	6.39	1.24	0.25	7.04	15.73	20.76	8.16	0.52	0.76	0.39	2.23	1.16	11.34
	Load cycled	HL	2.90	1.87	0.64	0.15	5.3	12.73	19.63	3.80	0.30	0.65	0.19	2.40	0.72	9.33
		BHL	2.89	2.54	0.88	0.17	4.3	15.06	17.38	5.85	0.39	0.87	0.34	3.50	1.36	10.56
EDTA + SB-ZnO	Control	HL	5.51	0.53	0.10	0.55	6.33	13.35	9.96	10.16	0.76	1.34	1.02	2.11	1.61	5.66
		BHL	6.07	-1.68	-0.28	0.45	10.11	15.17	13.49	17.81	1.17	1.12	1.32	1.50	1.76	3.67
	Load cycled	HL	2.63	3.97	1.51	0.43	3.6	11.94	6.09	3.53	0.30	1.96	0.58	3.32	0.98	7.18
		BHL	6.88	8.89	1.29	0.69	2.82	13.74	9.97	5.34	0.39	1.38	0.54	4.87	1.89	4.54
EDTA + SB-$ZnCl_2$	Control	HL	2.47	2.67	1.08	0.15	8.41	13.69	16.11	4.80	0.35	0.85	0.30	1.63	0.57	6.27
		BHL	4.68	4.55	0.97	0.25	9.59	18.38	18.79	11.86	0.65	0.98	0.63	1.92	1.24	8.71
	Load cycled	HL	4.75	1.85	0.39	0.18	5.94	16.85	26.88	7.74	0.46	0.63	0.29	2.84	1.30	5.25
		BHL	3.45	3.18	0.92	0.13	33.99	18.24	26.01	12.58	0.69	0.70	0.48	0.54	0.37	33.39

Abbreviations: A: Amide; Pyrid: Pyridinium; AGEs: Advanced glycation end products. EDTA: ethylenediaminetetraacetic acid.Peaks positions are expressed in cm^{-1}.

Table 4. Adhesive components of phosphoric and ethylenediaminetetraacetic acids-treated caries-affected dentin interfaces plus Single Bond adhesive application (PA+SB; EDTA+SB) measured at the hybrid layer.

		Degree of adhesive penetration		
		DC [1637/1608]	Bis-GMA [1113/A-I]	Other adhesive components [1450/1667]
PA + SB	Control	0.73	1.04	1.88
	Load cycled	0.95	0.80	1.31
PA + SB-ZnO	Control	1.61	0.59	2.50
	Load cycled	1.70	6.31	1.18
PA + SB-$ZnCl_2$	Control	0.20	8.58	12.94
	Load cycled	1.35	0.81	2.17
EDTA + SB	Control	0.52	3.51	7.23
	Load cycled	0.62	2.80	5.17
EDTA + SB-ZnO	Control	5.31	0.70	0.98
	Load cycled	2.22	6.31	1.73
EDTA + SB-$ZnCl_2$	Control	0.83	1.48	3.36
	Load cycled	0.58	1.73	3.47

Abbreviations: DC: Degree of conversion of adhesive; Bis-GMA: bisphenol A diglycidyl methacrylate.

Our results confirm that load cycling of caries-affected dentin surfaces conditioned with phosphoric acid or EDTA, and infiltrated with an etch-and-rinse adhesive doped with zinc oxide or zinc chloride promotes an increase of mineralization at the resin/caries-affected dentin interface. Crystals preferentially nucleated at intrafibrillar compartment when EDTA was used to pre-treat dentin.

Specimens treated with PA+SB-ZnO group attained higher both nanohardness (Hi) (Eq. 3) and Young's modulus (*Ei*) (Eq. 2) in comparison with the control group (PA+SB), at both hybrid layer (Fig. 1) and bottom of the hybrid layer (Fig. 2). Considering that the improvement of *Hi* and *Ei* is associated with a remineralizing effect, it can be assumed that the degree and quality of mineralization has been focused at intrafibrillar level, just where the lower fibrillar content of mineral is located (Balooch et al., 2008). Indeed, the extrafibrillar minerals act as a granular material that can withstand load, but in the absence of intrafibrillar mineralization. Intrafibrillar mineralization is the key factor to ensuring that collagen fibrils have the same high modulus of elasticity (*Ei*) and hardness (*Hi*) as occurs in natural biomineralized dentin (Balooch et al., 2008). Therefore, the increase of *Ei* and *Hi* of the partially demineralized collagen is directly related to the precipitation of minerals at the resin-dentin interface (Li et al., 2012), and more specifically at the intrafibrillar compartment (Balooch et al., 2008; Bertassoni et al., 2009), leading to functional remineralization. A relative advance of the remineralization front was observable throughout the Masson's trichrome images, at the resin-dentin interface, as some non-uniform and discontinuous zones that exhibited less pink and red areas below the adhesive layer were revealed (Fig. 4b). The most intense redder staining fringe was shown at the unload cycled samples treated with un-doped adhesive (Fig. 4a).

Specimens treated with PA+SB-ZnO and load cycled showed, in general, lower values in both nano-mechanical properties (*Hi* and *Ei*) (Figs. 1, 2) but higher relative mineral concentration (RMC) than the unloaded samples (Table 2a). These findings confirmed the increased mineralization at the extrafibrillar compartment, as only intrafibrillar mineralization accounts for the improvement of the nanomechanical properties (Bertassoni et al., 2009). The attained remineralization after using ZnO-doped adhesives in phosphoric acid-treated dentin was observed at the interface, as a growth of some new dentinal tubuli crossing the superficial demineralized dentin, indicating remineralization of peritubular and intertubular dentin (Fig. 4d), not observable in the unload cycled samples (Fig. 4c). In addition, an increase in the degree of mineralization related to the phosphate and carbonate groups at both hybrid layer and bottom of hybrid layer was also determined after Raman analysis (Table 2a) (Fig. 3.1g).

Multivariate analysis of Raman map images were produced by PCA (principal components analysis) and HCA (hierarchical cluster analysis) in the spectral range between 900 and 1900 cm^{-1}, in order to automatically distinguish different components at sub-nanostructural levels. This type of analysis allowed the interpretation of similarities and differences between the clusters of the samples by analyzing the PCA scores and loadings. The PCA loadings are combinations between Raman spectra of components of the sample that describe the biggest difference between spectra (Kunstar et al., 2012). HCA results reflected the chemical compounds and the spatial distribution of the main spectra, and showed three distinguishable different clustered groups in contiguous traces of the scatter plots, according to similar conditions of featuring (Vanna et al., 2015), where each cluster has been assigned a different color (Bonifacio et al., 2010). Thus, the corresponding PCA and HCA Raman images (clusters) and results (centroids) obtained at the interface of specimens treated with PA+SB-ZnO load

cycled (Figs. 6·b, 7·b) showed a generalized increase of the phosphate peak and mPPR (modified phosphate peak ratio) (Table 2a) at two out the three distinguishable centroids (HCA_1 and HCA_2) (red and green areas in Fig. 6·b), in comparison with the unload cycled specimens (Figs. 6·a and 7·a), indicating mineral gain. The main centroid (HCA_3) (Fig. 7·b, blue area in Fig. 6·b), which represents 50% of the variance slightly decreased the intensity of the phosphate peak (from ~18 to 15 intensity counts) after load cycling. This formed mineral gave rise to Raman bands characteristics of an enriched carbonated apatite (Wang et al., 2009) (~1.9 and 1.7 folds at the hybrid layer and bottom of the hybrid layer, respectively), in comparison with the unloaded specimens (Fig. 3·1g). Changes in the spectral region of carbonate content have been ascribed to either growth of a carbonate peak or changes in the phosphate peak in response to the presence of carbonate in the lattice (Awonusi et al., 2007). The presence of a prominent carbonate band around 1070 cm^{-1}correlated with the increased degree of carbonate substitution in the lattice structure of apatite (Salehi et al., 2013), and match with the narrowing full-width half-maximum (FWHM) of the phosphate ν_1 peak (at ca. 960 cm^{-1}), after load cycling (Table 2a). FWHM reflects a broad augmentation of crystallographic maturity, crystallinity, in minerals, at the interface (Schwartz et al., 2012) (Table 2a), and was evidenced at Fig. 3.1g. The term crystallinity refers to the order of a solid where a highly crystalline material displays long range sequence among its component atoms, and amorphous material. The increase in crystallinity (*i.e.*, crystallographic maturity) at 961 cm^{-1} suggested the presence of hydroxyapatite crystals exhibiting a relative lower degree of imperfections and substitutions (Wang et al., 2009).

On the contrary, samples of carious dentin treated with PA+SB-$ZnCl_2$ performed dissimilar, as load cycling did not affect nanohardness (*Hi*) at hybrid layer nor bottom

of hybrid layer, and the Young's modulus decreased at the bottom of the hybrid layer after load cycling (Figs. 1, 2). These results became associated with a poor remineralization at the intrafibrillar compartment (Balooch et al., 2008), *i.e*, simple precipitation of mineral (Xu et al., 2013). Masson's trichrome staining observations confirmed a scarce variation in the red intensity, as a consequence of the poor remineralization potential, in general (Figs. 4e, 4f). Furthermore, this redder coloration was also the result of the lower degree of conversion, though greater adhesive (Bis-GMA and HEMA/Ratio1450/1667) penetration, that attained this group in spite of using phosphoric acid or EDTA for conditioning (Table 4).

Nevertheless, the relative presence of minerals (Table 2a) (Fig. 3.1f) and the modified phosphate peak ratio (mPPR) resulted higher, after load cycling (Table 2a). Both FWHM (full-width half-maximum) and GMC (gradient of mineral content) decreased at the bonded interface, ~1.1 and 2 fold, respectively, if compared with the control group (Table 3 a) (Fig. 3.1g). GMC, as result, indicated lower carbonate substitution for phosphate, and in junction with the diminished FWHM pointed out higher maturity and crystallinity, associated with a decrease of amorphous calcium phosphate compounds (Karan et al, 2009; Schwartz et al, 2012).

Collagen crosslinking is affected by the tissue maturation as well as the degree of mineralization, providing information about the structure and molecular interactions of complexes biomolecules (Xu and Wang, 2011; Saito et al., 2006). Ratios concerning the crosslinking of collagen reflected a movement toward higher frequencies after load cycling, denoting a general rise at 1032 (pyridinium), 1032/1003, and 1003/1450 cm^{-1} (phenyl/CH_2) at the bonded interface when SB-ZnO or SB-$ZnCl_2$ were applied in phosphoric acid-treated dentin (Table 2b). The Raman band around 1032 cm^{-1} is assigned to the pyridinium ring vibration, and poses a rapid screening method to check

the cross-linking capability of collagen, as the relative intensity of this peak increases after the crosslinking formation (Xu and Wang, 2011). The ratios 1032/1003 cm^{-1} and 1003/1450 cm^{-1} can also be used to measure the crosslinking reaction of collagen, corresponding to the non-reducible/reducible cross-link ratio (Ager et al., 2005); the higher the ratio is, the greatest the extend of collagen crosslinking (Wang et al, 2009; Xu and Wang, 2012). In general, mechanical loading may have stimulated the conversion of keto-amines (immature cross-links), promoting a sharper and accentuated peak with a notable shift at 1032 cm^{-1}, at both HL and BHL after using both Zn-doping compounds (Table 2b) (Fig. 3.1g). The high relative intensity peak corresponding to the pyridinium ring may be, in general, associated with a non-reducible crosslinking formation, demonstrating that the first remineralization is intrafibrillar. This was stated by the present spectra of crystallinity which reflects the Table 2a, confirming that collagen, even in the case of caries-affected dentin is an active scaffold which facilitate the formation of oriented crystalline hydroxyapatite inside the fibrils (Cölfen, 2010; Nudelman et al., 2010). The spectra corresponding to these groups were quite similar (Figs. 7·b, 7·d), in spite of the overlapped plots attained between 1150 and 1450 cm^{-1} of the Raman shift at the carious dentin treated with SB-$ZnCl_2$ (Fig. 7·d). When specimens were treated with PA+SB-$ZnCl_2$ and load cycled, HCA_1 (loadings in Figs. 6·d, 7·d), represented 49% of the variance of the dataset, performed as the first principal component of the spectra and mainly defined the general performance of the loading spectrum, in junction with the cluster HCA_3, which represents 44% of the variance. According to the false-color map of Fig. 6·d, the homogenizing effect that the load cycling promotes at the resin-dentin interface may be appreciated, in comparison with the unload group (Fig. 6·c) or with the group where PA+SB-ZnO was used (Fig. 6·b). These results comply, partially with Kuboki et al. (1981), who determined by electron

microscopy that crosslinking of collagen remained in the caries-affected dentin, and collagen fibrils were showing the typical banding structure of sound dentin. Pentosidine, is the main AGE (advance glycation end products) component (Salehi et al., 2013). Its presence strongly suggest ribose or ribonucleotide metabolites as precursors (Sell and Monnir, 1989). Pentosidine has been demonstrated to contribute to the age-related stiffening of tissues by cross-linking of the extracellular matrix, and may serve as a molecular marker of the aging process (Sell and Monnir, 1989). Pentosidine Raman signal augmented ~1.5 fold when samples were treated with PA+SB-$ZnCl_2$ and load cycled (Figs. 3·1g, 7d), but diminished ~1.4 fold when PA+SB-ZnO was used (Table 2b) (Figs. 3·1g, 7b). This higher intensity peak at the interface of specimens treated with $ZnCl_2$ indicates the presence of a more advanced decayed organic substrate (Sell and Monnir, 1989), but with greater potential for further remineralization, as scaffolding of collagen (amide III/AGEs-pentosidine) (Salehi et al, 2013) increased ~1.5 fold after load cycling (Table 2b). Peaks at 1340 cm^{-1} (α-helices), also augmented in samples treated with PA+SB-$ZnCl_2$ (Figs. 3·1g, 7d), denoting a greater sensitivity to molecular orientation in order to enhance further crystallization (Wang et al., 2009), (Table 2b). These maps are in satisfactory agreement with the hystopathological results described in Figs. 4d and 4f.

For the most part, when caries-affected dentin was EDTA-treated, resin-infiltrated and load cycled, Zn-doped specimens clearly attained higher *Hi* and *Ei* at both hybrid layer and bottom of hybrid layer, in comparison with the unloaded specimens (Figs. 1, 2), as a consequence of intrafibrillar or functional mineralization (Balooch et al., 2008). Functional remineralization is the result of a process that yields recovery of physical and chemical properties otherwise lost due to disease (Burwell et al., 2012). At his stage, the first null hypothesis which reads “functional remineralization of the resin-

caries affected dentin interface obtained with zinc-doped adhesives is not produced neither influenced by the different tested etching procedures, after load cycling" must also be rejected. Masson's trichrome stained sections of EDTA-treated and Zn-doped resin-dentin infiltrated specimens showed a much thinner unprotected collagen layers (Figs. 5d, 5f) than that seen for the control group (EDTA+SB) (Figs. 5a, 5b), which additionally showed lower mechanical properties (Figs. 1, 2), lower relative presence of minerals, and lower crystallinity (Table 3a) with an augmented presence of amorphous calcium phosphate after load cycling. It is important to place emphasis on that amorphous calcium phosphate provides a local ion-rich environment which is considered favorable for *in situ* generation of prenucleation clusters, succeeding further dentin remineralization (Liu et al., 2011). On the contrary, if crystalline calcium phosphates are formed, they will have long degradation times, requiring months or even years to provide ions to the remineralizing media (Rezwan et al., 2006). The biodegradability of these new mineral formations depends on many parameters such as crystallinity, porosity, chemical purity, surface roughness, pH in the media, and other solubilized ions present at the oral environment (Cochrane et al., 2010; Hoppe et al., 2011). The provoqued broadening suggests the state of hydroxyapatite as ultrafine nano-crystalline (Almahdy et al., 2012). The association between broadening and poor crystallinity denotes the presence of, *i)* higher degrees of impurities and amorphous phase, with decreased chemical stability (Moshaverinia et al., 2008), and creates biogenic apatites that are characterized by low degree of crystallinity and non-stoichiometry (Ager et al., 2005); and *ii)* increase in the crystal disorders of hydroxyapatite, which has been linked to lower mechanical properties, likely related to increase solubility (Low, 2004). The broad peaks are usually attributed to the extremely small dimensions of the hydroxyapatite crystallites, which is presumably due to the

limited space available for intrafibrillar mineral. Broad diffractions peaks could also arise from weak long-range periodic correlations, or from crystal strain (Olszta et al., 2007). On the whole, light microscopy observations demonstrated non-exposed and un-enveloped-stained collagen network at the bottom of the hybrid layer after load cycling, confirming any demineralization sight underside the resin-caries-affected dentin inter-diffusion zone (Figs. 5d, 5f).

The functional and histological remineralization in samples treated with EDTA+SB-ZnO load cycled, determined by the nano-mechanical test and the light microscopy study respectively, corresponded with an augmentation of the relative presence of minerals concerning the increases of, a) the peak height of phosphate (~1.2 fold at HL and ~1.3 fold at BHL) (Figs. 3.2d, 3.2g), b) area of phosphate (~1.4 fold at HL and ~1.6 fold at BHL), c) modified phosphate peaks ratio (mPPR) (~1.2 fold at HL and ~1.4 fold at BHL), and d) relative mineral concentration (RMC) (~2.5 fold at HL and ~1.2 fold at BHL) (Table 3a). The false-color map provided by the HCA images appeared with disaggregated granular-shaped red cluster, in the upper half of the map, at the interfaces promoted with EDTA+SB-ZnO load cycled (Fig. 6·f), having a higher proportion of phosphate (961 cm^{-1}) and carbonate (1071 cm^{-1}). On the other hand, HCA results showed an almost totally overlapped spectra (Fig. 7·f) and more balanced variances, *i.e*, 16/32/52% after load cycling in comparison with 9/20/71% in the unload cycled specimens (Fig. 7·e), at HCA_1, HCA_2 and HCA_3, respectively. The increase of crystallinity (reduced FWHM) was attained at the expense of HCA_1 and HCA_2 (red and green centroids), which showed the lowest variances (Fig. 7·f). The smaller the variance-weighted between the clusters was, the more they resemble each other (Kunstar et al., 2012). Specimens treated with EDTA+SB-$ZnCl_2$ followed similar trend after load cycling, as the peak height of phosphate (~5.78 fold at HL and ~1.73 fold at

BHL), the area of phosphate (~4.16 fold at HL and ~1.37 fold at BHL), the modified phosphate peaks ratio (mPPR) (~6.14 fold at HL and ~1.72 fold at BHL), and the relative mineral concentration (RMC) (~3.00 fold at HL and ~2.34 fold at BHL) also increased (Table 3a).

HCA_2 and HCA_3 (green and blue centroids) shared similar plot, except at the phosphate band (961 cm^{-1}) in the unload cycled specimens (Fig. 7·g), but overlapped with HCA_1 after load cycling (Fig. 7·h). The fact that these two groups (HCA_1 and HCA_2 + HCA_3) (Fig. 7·g) are much more dispersed than at the loaded samples treated with SB-$ZnCl_2$ (Fig. 7·h), confirms the relative high level of heterogeneity of these type of dentin, mostly due to a different level of maturation of each measured cluster (Vanna et al., 2015). The HCA_3 centroid, the first principal component (loadings in Figs. 6·h and 7·h), which described 45% of the variance of the entire dataset, defined three main differences respect to the other two principal grouped centroids, as *i)* the low height of the phosphate peak (961 cm^{-1}) (~ lower than 18 intensity counts), *ii)* the inverted peak corresponding to the pyridinium peak (1032 cm^{-1}), associated with a reduction in crosslinking capability (Jastrzebska et al., 2003), and *iii)* the scarce peak fitting procedure on amide I band of the spectra showing lower changes in the secondary structure of proteins (Tosi et al, 2011).

The organic components in samples treated with EDTA+SB-ZnO and SB-$ZnCl_2$ showed, in general, a lack of conformation and organization of collagen, as resulted from a poor collagen matrix quality (Ratio Amide I/CH_2) (Figs. 3·2g, 7f, 7h) (Xu and Wang 2012, Salehi et al., 2013). The ratio Amide I/CH_2 reduction also hindered the scaffolding (Salehi et al., 2013) (Table 3b) (Fig. 3.2g). Nevertheless, the molecular orientation, *i.e.*, α-helices (1340 cm^{-1}) augmented at the interface after loading (Table 3b), enhancing further crystallization (Wang et al., 2009), fundamentally at the

specimens treated with SB-$ZnCl_2$ that attained a decreased of FWHM at the hybrid layer and at the bottom of the hybrid layer, after load cycling (Table 3a). Nature of collagen resulted favorable after mechanical loading when specimens were treated with EDTA+SB-$ZnCl_2$, as peak intensities corresponding to A-III, CH_2, A-1 and ratio A-I/A-III were towards higher frequencies, indicating that organic components were well organized (Xu and Wang, 2012) for promoting apatite nucleation (Toledano et al., 2014c) (Table 3b) (Figs. 3·2g, 7·h). It is noteworthy the similar trend that attained the three main centroids, in load cycled samples after observing the HCA results (Fig. 7·h), especially the CH_2 peaks (1450 cm^{-1}), that showed the highest homogeneity when molecular conformation of the polypeptide chains was assessed (Xu and Wang, 2012).

It has been demonstrated that intermittent compressive load stimulates the proteic synthesis and alkaline phosphatase activity *in vivo* and *in vitro* (Lozupone et al, 1996). Alkaline phosphatase, present at all mineralization sites, hydrolyzes phosphate esters producing free phosphate, and thus apatite supersaturation (Posner et al., 1986). Furthermore, the mineral-inductive capacity of partially demineralized dentin may be explained, in addition, by the small but definitive fraction of remaining polyanionic proteins (phosphoproteins), strongly attached to the collagenous matrix. The peptides responsible for mineral induction are located between the two collagen binding sites. Removing, by different decalcifying agents, the soluble portion of the organic matrix, which contains phosphoproteins, it is essential to remineralization of demineralized dentin. Inmunohistological evidences suggest that the antigenicity of type I collagen and proteoglycans are altered in caries-affected dentin (Suppa et al., 2006). However, incorporating zinc into the chemical formulation of resin adhesives increases the potential for intrafibrillar remineralization at partially demineralized collagen matrices of caries-affected dentin, especially when specimens were treated with PA+SB-ZnO.

After load cycling, the most pronounced remineralizing effect occurred when caries-affected substrata were EDTA-treated and then load cycled. The rising minimally invasive approach in the treatment of dentin caries brings forth a need to assess models that can help to elucidate these aspects.

To sum up, mechanical loading of caries-affected dentin surfaces conditioned with phosphoric acid or EDTA, and infiltrated with an etch-and-rinse adhesive doped with both zinc oxide and zinc chloride inducts an increase of mineralization at the resin/caries-affected dentin interface. Caries-affected dentin surfaces conditioned with phosphoric acid and infiltrated with adhesive-ZnO doped promoted the growing of some new dentinal tubuli crossing the superficial demineralized dentin, indicating remineralization of peritubular and intertubular dentin. This group, after load cycling formed mineral which gave rise to Raman bands characteristics of an enriched carbonated apatite with augmented crystallographic maturity in crystals, at the interface. $ZnCl_2$-doped adhesive performed dissimilar, as load cycling did not affect nanohardness and, as result, a poor remineralization potential was described, at intrafibrillar level. After load cycling, both the relative presence of minerals and the modified phosphate peak ratio increased, but crystallinity and the gradient of mineral content diminished at the interface. Ratios concerning the crosslinking of collagen reflected a movement toward higher frequencies after load cycling, when ZnO or $ZnCl_2$ were included in SB. The favorable nature of collagen for scaffolding and further mineralization was also observed at both resin-doped-CAD interfaces after load cycling. When caries-affected dentin was EDTA-treated, resin-infiltrated and load cycled, Zn-doped specimens clearly attained higher nanomechanical properties. As a consequence, much thinner unprotected collagen layers than those seen for the control group, could be observed. Even more, many samples unveiled any demineralization sight at the bottom of the resin-caries-

affected dentin inter-diffusion zone. This mineral precipitation became associated to an augmentation of the relative presence of minerals. Additionally, the organic components permitted to observe a lack of conformation and organization of collagen. This fact resulted from a poor collagen matrix quality, still indicating the presence of a decayed organic substrate, though producing an adequate matrix organization to promote apatite nucleation.

These are, to the best of our knowledge, the only available results from nano-indentation, Raman spectroscopy and Masson's trichrome staining combined methodologies destined to analyze Zn-doped etch-and-rinse adhesive/caries-affected dentin interfaces submitted to mechanical loading. These outcomes are important, because they provide information on bio-physic-chemical structure of Zn-doped resin-carious dentin treated for essential clinical applications. Relative to complementary experimental techniques that ultimately illustrate the clinical answer of carious dentin, Field-emission SEM (FESEM), dark-field TEM (DF-TEM), High Resolution TEM (HRTEM), Scanning Transmission Electron Microscopy (STEM) and micro-XRD (μ-XRD), and fuzzy c-means cluster analysis (FCA) should be incorporated into our methodology, for future strategies of research. Relative to FCA, a "hard" clustering method such as HCA, when forced to partition the map into distinct clusters, might fail to describe a "soft" transition between two or more areas of the sample, such as a smooth gradient of one biochemical component. To achieve a better description of continuous variation in future actions, FCA (soft) could be employed in combination with HCA (hard). On the other hand, once characterized these new crystals that appeared at the carious dentin surface after mechanical loading, it might be interesting to develop new composites based on this hydroxyapatite, by bio-monitoring these data. Applying advanced technologies, both biofunctionality and biocompatibility studies

should be carried out by using these starting crystals for the production of hydroxyapatite for therapeutic dental applications in regions of demineralized dentin. This approach also deserves future research.

4. CONCLUSIONS.

1. Caries-affected dentin specimens conditioned with phosphoric acid and infiltrated with a ZnO-doped etch-and-rinse adhesive attained the highest nano-mechanical properties; even when these properties decreased after load cycling, they still remained high above than those obtained in the rest of the experimental groups. Their mineral concentration augmented as a consequence of simple precipitation, improvement of the structure of collagen and an enriched crystallographic maturity, accountable for histological and functional remineralization.

2. Nano-mechanical properties were not altered when caries-affected dentin surfaces conditioned with phosphoric acid, infiltrated with a $ZnCl_2$-doped etch-and-rinse adhesive were submitted to load cycling, in comparison with the unloaded samples, though both crystalline and amorphous minerals augmented in junction with better molecular orientation, at the resin-dentin interface.

3. Load cycling increased the mechanical properties when EDTA-treated caries-affected dentin was infiltrated with a ZnO or $ZnCl_2$-doped etch-and-rinse adhesive, promoting both histological and functional remineralization, as a result of increased mineral concentration and intrafibrillar mineral precipitation, respectively, though the degree of carbonate substitution decreased in the lattice structure of apatite, in general, producing amorphous calcium phosphate together with an improved quality of collagen, in nature.

4. Caries-affected dentin specimens EDTA-treated and infiltrated with a $ZnCl_2$-doped etch-and-rinse adhesive, and submitted to mechanical loading attained improved crystallographic maturity and higher carbonate gain than ZnO-doped samples, presenting better chemical stability, but relative biodegradability as result of the lower degree of carbonate substitution in comparison with the unloaded specimens.

ACKNOWLEDGMENTS

Project MAT2014-52036-P supported by the Ministry of Economy and Competitiveness (MINECO) and European Regional Development Fund (FEDER). In addition, the authors would like to thank the technical support of PhD Inmaculada Cabello for sample preparation and manuscript edition.

The authors affirm that no actual or potential conflict of interest including any financial, personal or other relationships with other people or organizations within three years of beginning the submitted work that could inappropriately influence, or be perceived to influence, their work. Any other potential conflict of interest is disclosed.

REFERENCES

Ager, J.W., Nalla, R.K., Breeden, K.L., Ritchie, R.O., 2005. Deep-ultraviolet Raman spectroscopy study of the effect of aging on human cortical bone. J. Biomed. Opt. 10, 034012.DOI:10.1117/1.1924668

Almahdy, A., Downey, F.C., Sauro, S., Cook, R.J., Sherriff, M., Richards, D., Watson, T.F., Banerjee, A., Festy, F., 2012. Microbiochemical analysis of carious dentine using Raman and fluorescence spectroscopy. Caries Res. 46, 432-440. DOI: 10.1159/000339487

Angker, L., Swain, M.V., 2006. Nanoindentation: Application to dental hard tissue investigations. J. Mater. Res. 21, 1893-1905.DOI: 10.1557/JMR.2006.0257

Awonusi, A., Morris, M.D., Tecklenburg, M.M.J., 2007. Carbonate assignment and calibration in the Raman spectrum of apatite. Calcif. Tissue Int. 81, 46–52. DOI: 10.1007/s00223-007-9034-0

Balooch, M., Habelitz, S., Kinney, J.H., Marshall, S.J., Marshall, G.W. Mechanical properties of mineralized collagen fibrils as influenced by demineralization. J. Struct. Biol. 2008, 162, 404-410. DOI: 10.1016/j.jsb.2008.02.010

Bertassoni, L.E., Habelitz, S., Kinney, J.H., Marshall, S.J., Marshall, G.W. Jr., 2009. Biomechanical perspective on the remineralization of dentin. Caries Res. 43, 70-77. DOI: 10.1159/000201593

Bertassoni, L.E., Stankoska, K., Swain, M.V., 2012. Insights into the structure and composition of the peritubular dentin organic matrix and the lamina limitans. Micron. 43, 229-236. DOI: 10.1016/j.micron.2011.08.003

Bertini, I., Fragai, M., Luchinat, C., Melikian, M., Toccafondi, M., Lauer, J.L., Fields, G.B., 2012. Structural basis for matrix metalloproteinase 1-catalyzed collagenolysis. J. Am. Chem. Soc. 134, 2100-2110. DOI: 10.1021/ja208338j

Bonifacio, A., Beleites, C., Vittur, F., Marsich, E., Semeraro, S., Paoletti, S., Sergo V., 2010. Chemical imaging of articular cartilage sections with Raman mapping, employing uni- and multi-variate methods for data analysis. Analyst 135, 3193-3204. DOI: 10.1039/c0an00459f

Burwell, A.K., Thula-Mata, T., Gower, L.B., Habelitz, S., Kurylo, M., Ho, S.P., Chien, Y.C., Cheng, J., Cheng, N.F., Gansky, S.A., Marshall, S.J., Marshall, G.W., 2012. Functional remineralization of dentin lesions using polymer-induced liquid-precursor process. PLoS One7, e38852. DOI: 10.1371/journal.pone.0038852

Carrilho, M.R., Geraldeli, S., Tay, F., de Goes, M.F., Carvalho, R.M., Tjäderhane, L., Reis, A.F., Hebling, J., Mazzoni, A., Breschi, L., Pashley, D., 2007. In vivo preservation of the hybrid layer by chlorhexidine. J. Dent. Res. 86, 529-533. DOI: 10.1177/154405910708600608

Chaussain-Miller, C., Fioretti, F., Goldberg, M., Menashi, S., 2006. The role of matrix metalloproteinases (MMPs) in human caries. J. Dent. Res. 85, 22-32. DOI: 10.1177/154405910608500104

Cochrane, N.J., Cai, F., Huq, N.L., Burrow, M.F., Reynolds, E.C., 2010. New approaches to enhanced remineralization of tooth enamel. J. Dent Res. 89, 1187-1197. DOI: 10.1177/0022034510376046

Cölfen, H., 2010.Biomineralization: A crystal-clear view. Nat. Mater. 9, 960–961. DOI: 10.1038/nmat2911

Daood, U., Iqbal, K., Nitisusanta, L.I., Fawzy, A.S., 2013. Effect of chitosan/riboflavin modification on resin/dentin interface: spectroscopic and microscopic investigations. J. Biomed. Mater. Res. Part A 101, 1846–1856. DOI: 10.1002/jbm.a.34482

De Munck, J., Van Landuyt, K., Peumans, M., Poitevin, A., Lambrechts, P., Braem, M., Van Meerbeek, B., 2005. A critical review of the durability of adhesion to tooth tissue: methods and results. J. Dent. Res. 84, 118–132. DOI: 10.1177/154405910508400204

Dousseau, F., Pézolet, M., 1990. Determination of the secondary structure content of proteins in aqueous solutions from their amide I and amide II infrared bands. Comparison between classical and partial least-squares methods. Biochemistry 29, 8771–8779. DOI: 10.1021/bi00489a038

Erhardt, M.C., Toledano, M., Osorio, R., Pimenta, L.A., 2008. Histomorphologic characterization and bond strength evaluation of caries-affected dentin/resin interfaces: effects of long-term water exposure. Dent. Mater 24, 786-798. DOI: 10.1016/j.dental.2007.09.007

Frankenberger, R., Pashley, D.H., Reich, S.M., Lohbauer, U., Petschelt, A., Tay, F.R., 2005. Characterisation of resin-dentine interfaces by compressive cyclic loading. Biomaterials 26, 2043-2052. DOI:10.1016/j.biomaterials.2004.07.003

Fratzl, P., Gupta, H.S., Paschalis, E.P., Roschger, P., 2004. Structure and mechanical quality of the collagen-mineral nano-composite in bone. J. Mater. Chem. 14, 2115–2123. DOI: 10.1039/B402005G

Fusayama, T., 1979. Two layers of carious dentin; diagnosis and treatment. Oper. Dent. 4, 63-70.

Habelitz, S., Balooch, M., Marshall, S.J., Balooch, G., Marshall Jr, G.W., 2002. In situ atomic force microscopy of partially demineralized human dentin collagen fibrils. J. Struct. Biol. 138, 227-236. DOI: 10.1016/S1047-8477(02)00029-1

Haj-Ali, R., Walker, M., Williams, K., Wang, Y., Spencer, P., 2006. Histomorphologic characterization of noncarious and caries-affected dentin/adhesive interfaces. J. Prosthodont. 15, 82-88. DOI: 10.1111/j.1532-849X.2006.00079.x

Han L., Grodzinsky A.J., Ortiz, C., 2011. Nanomechanics of the cartilage extracellular matrix. Annu. Rev. Mater. Res. 1, 133-168. DOI: 10.1146/annurev-matsci-062910-100431

Hoppe, A., Güldal, N.S., Boccaccini, A.R., 2011. A review of the biological response to ionic dissolution products from bioactive glasses and glass-ceramics. Biomaterials 32, 2757-2774. DOI: 10.1016/j.biomaterials.2011.01.004

Jastrzebska M, Wrzalik R, Kocot A, Zalewska-Rejdak J, Cwalina B., 2003. Raman spectroscopic study of glutaraldehyde-stabilized collagen and pericardium tissue. J. Biomater. Sci. Polym. Ed. 14, 185-97. DOI: 10.1163/156856203321142605

Karan, K., Yao, X., Xu, C., Wang, Y., 2009. Chemical profile of the dentin substrate in non-carious cervical lesions. Dent. Mater. 25, 1205-1212. DOI: http://dx. DOI.org/10.1016/j.dental.2009.04.006

Kinney J.H., Nalla R.K., Pople J.A., Breunig T.M., Ritchie R.O., 2005. Age-related transparent root dentin: mineral concentration, crystallite size, and mechanical properties. Biomaterials 26, 3363–3376. DOI: 10.1016/j.biomaterials.2004.09.004

Koibuchi, H., Yasuda, N., Nakabayashi, N., 2001. Bonding to dentin with a self-etching primer: the effect of smear layers. Dent. Mater. 17, 122-126. DOI: 10.1016/S0109-5641(00)00049-X

Kokubo, T., Kushitani, H., Sakka, S., Kitsugi, T., Yamamuro, T., 1990. Solutions able to reproduce in vivo surface-structure changes in bioactive glass-ceramic A-W. J. Biomed. Mater. Res. 24, 721-734. DOI: 10.1002/jbm.820240607

Kuboki, Y., Tsuzaki, M., Sasaki, S., Liu, C.F., Mechanic, G.L. 1981. Location of the intermolecular cross-links in bovine dentin collagen, solubilization with trypsin and isolation of cross-link peptides containing dihydroxylysinonorleucine and pyridinoline. Biochem. Biophys. Res. Commun. 102, 119-126. DOI: 10.1016/0006-291X(81)91497-2

Kunstar, A., Leijten, J., van Leuveren, S., Hilderink, J., Otto, C., van Blitterswijk, C.A., Karperien, M., van Apeldoorn, A.A., 2012. Recognizing different tissues in human fetal femur cartilage by label-free Raman microspectroscopy. J. Biomed. Opt.17, 116012. DOI: 10.1117/1.JBO.17.11.116012

Li, Y., Thula, T.T., Jee, S., Perkins, S.L., Aparicio, C., Douglas, E.P., Gower, L.B., 2012. Biomimetic mineralization of woven bone-like nanocomposites: role of collagen cross-links. Biomacromolecules. 13, 49-59. DOI: 10.1021/bm201070g

Liu, Y., Mai, S., Li, N., Yiu, C.K., Mao, J., Pashley, D.H., Tay, F.R., 2011. Differences between top-down and bottom-up approaches in mineralizing thick, partially demineralized collagen scaffolds. Acta Biomater. 7, 1742-1751. DOI: 10.1016/j.actbio.2010.11.028

Liu, Y., Yao, X., Liu, Y.W., Wang, Y., 2014. A Fourier transform infrared spectroscopy analysis of carious dentin from transparent zone to normal zone. Caries Res. 48, 320-329. DOI: 10.1159/000356868

Low, I.M., 2004. Depth-profiling of crystal structure, texture, and microhardness in a functionally graded tooth enamel. J. Am. Ceram. Soc. 87, 2125*–2131. DOI*: 10.1111/j.1151-2916.2004.tb06369.x

Lozupone, E., Palumbo, C., Favia, A., Ferretti, M., Palazzini, S., Cantatore, F.P., 1996. Intermittent compressive load stimulates osteogenesis and improves osteocyte viability in bones cultured "in vitro". Clin. Rheumatol. 15, 563-572.

Lynch, R.J., Churchley, D., Butler, A., Kearns, S., Thomas, G.V., Badrock, T.C., Cooper, L., Higham, S.M., 2011. Effects of zinc and fluoride on the remineralisation of artificial carious lesions under simulated plaque fluid conditions. Caries Res. 45, 313-322. DOI: 10.1159/000324804

Marangos, O., Misra, A., Spencer, P., Bohaty, B., Katz, J.L., 2009. Physico-mechanical properties determination using microscale homotopic measurements: application to sound and caries-affected primary tooth dentin. Acta Biomater. 5, 1338-1348. DOI: 10.1016/j.actbio.2008.10.023

Milly, H., Festy, F., Watson, T.F., Thompson, I., Banerjee, A., 2014. Enamel white spot lesions can remineralise using bio-active glass and polyacrylic acid-modified bio-active glass powders. J. Dent. 42, 158-166. DOI: 10.1016/j.jdent.2013.11.012

Misra, A., Spencer, P., Marangos, O., Wang, Y., Katz, J.L., 2004. Micromechanical analysis of dentin/adhesive interface by the finite element method. J. Biomed. Mater. Res. B Appl. Biomater. 70, 56-65. DOI: 10.1002/jbm.b.30012

Moshaverinia, A., Ansari, S., Moshaverinia, M., Roohpour, N., Darr, J.A., Rehman, I., 2008. Effects of incorporation of HAp and fluoroapatite nanobioceramics into conventional glass ionomer cements (GIC). Acta Biomater. 4, 432–440. DOI: 10.1016/j.actbio.2007.07.011

Nakabayashi, N., 1992. The hybrid layer: a resin-dentin composite. Proc. Finn. Dent. Soc. 88 (Suppl 1), 321-329.

Nudelman, F., Pieterse, K., George, A., Bomans, P.H., Friedrich, H., Brylka, L.J., Hilbers, P.A.J., de With, G., Sommerdijk, N.A.J. M., 2010.The role of collagen in

bone apatite formation in the presence of hydroxyapatite nucleation inhibitors. Nat. Mater. 9, 1004–1009. DOI: 10.1038/nmat2875

Oliver, W.C., Pharr, G.M., 1992. An improved technique for determining hardness and elastic modulus using load and displacement sensing indentation experiments. J. Mater. Res. 7, 1564-1583. DOI: 10.1557/JMR.1992.1564

Olszta, M.J., Cheng X.G., Jee, S.S., Kumar, R., Kim, Y.Y., Kaufman, M.J., Douglas, E. P., Gower, L.B., 2007. Bone structure and formation: A new perspective. Mat. Sci. Eng. R. 58, 77-116. DOI: 10.1016/j.mser.2007.05.001

Osorio, R., Erhardt, M.C., Pimenta, L.A., Osorio, E., Toledano, M., 2005. EDTA treatment improves resin-dentin bonds' resistance to degradation. J. Dent. Res. 84, 736-40. DOI: 10.1177/154405910508400810

Osorio, R., Yamauti, M., Osorio, E., Ruiz-Requena, M.E., Pashley, D., Tay, F., Toledano, M., 2011a. Effect of dentin etching and chlorhexidine application on metalloproteinase-mediated collagen degradation. Eur. J. Oral Sci. 119, 79-85. DOI: 10.1111/j.1600-0722.2010.00789.x.

Osorio, R., Yamauti, M., Osorio, E., Ruiz-Requena, M.E., Pashley, D.H., Tay, F.R., Toledano, M., 2011b. Zinc reduces collagen degradation in demineralized human dentin explants. J. Dent. 39, 148-153. DOI: 10.1016/j.jdent.2010.11.005

Poon, B., Rittel, D., Ravichandran, G., 2008. An analysis of nanoindentation in linearly elastic solids. Int. J. Solids Struct. 45, 6018–6033. DOI: 10.1016/j.ijsolstr.2008.07.021

Posner, A.S., Blumenthal, N.C., Boskey, A.L., 1986. Model of aluminum-induced osteomalacia: inhibition of apatite formation and growth. Kidney Int. Suppl.18, S17-S19.

Rezwan, K., Chen, Q.Z., Blaker, J.J., Boccaccini, A.R., 2006. Biodegradable and bioactive porous polymer/inorganic composite scaffolds for bone tissue engineering. Biomaterials 27, 3413-3431. DOI:10.1016/j.biomaterials.2006.01.039

Ryou, H., Niu, L.N., Dai, L., Pucci, C.R., Arola, D.D., Pashley, D.H., Tay, F.R., 2011. Effect of biomimetic remineralization on the dynamic nanomechanical properties of dentin hybrid layers. J. Dent. Res. 90, 1122-1128. DOI: 10.1177/0022034511414059

Saito, M., Fujii, K., Marumo, K., 2006. Degree of mineralization-related collagen crosslinking in the femoral neck cancellous bone in cases of hip fracture and controls. Calcif. Tissue Int. 79, 160-168. DOI: 10.1007/s00223-006-0035-1

Salehi, H., Terrer, E., Panayotov, I., Levallois, B., Jacquot, B., Tassery, H., Cuisinier, F., 2013. Functional mapping of human sound and carious enamel and dentin with Raman spectroscopy. J. Biophotonics 6, 765-774. DOI: 10.1002/jbio.201200095

Schwartz, A.G., Pasteris, J.D., Genin, G.M., Daulton, T.L., Thomopoulos, S., 2012. Mineral distributions at the developing tendon enthesis. PLoS One 7, e48630. DOI: 10.1371/journal.pone.0048630

Sell, D.R., Monnir, V.M., 1989. Structure elucidation of a senescence cross-link from human extracellular matrix. Implication of pentoses in the aging process. J. Biol. Chem. 264, 21597-21602.

Spencer, P., Wang, Y., 2001. X-ray photoelectron spectroscopy (XPS) used to investigate the chemical interaction of synthesized polyalkenoic acid with enamel and synthetic hydroxyapatite. J. Dent. Res. 80, 1400-1401. DOI: 10.1177/00220345010800050101

Suppa, P., Ruggeri, A. Jr., Tay, F.R., Prati, C., Biasotto, M., Falconi, M., Pashley, D.H., Breschi, L., 2006. Reduced antigenicity of type I collagen and proteoglycans in

sclerotic dentin. J Dent Res.85, 133-137. Erratum in: J Dent Res. 2006, 85, 384. DOI: 10.1177/154405910608500204

Takatsuka, T., Tanaka, K., Iijima, Y., 2005. Inhibition of dentine demineralization by zinc oxide: in vitro and in situ studies. Dent. Mater. 21, 1170-1177. DOI: 10.1016/j.dental.2005.02.006

Toledano, M., Aguilera, F.S., Cabello, I., Osorio, R., 2014b. Remineralization of mechanical loaded resin-dentin interface: a transitional and synchronized multistep process. Biomech. Model. Mechanobiol. 13, 1289-1302. DOI: 10.1007/s10237-014-0573-9

Toledano, M., Aguilera, F.S., Osorio, E., Cabello, I., Toledano-Osorio, M., Osorio R., 2015. Bond strength and bioactivity of Zn-doped dental adhesives promoted by load cycling. Microsc. Microanal. 21, 214-230. DOI: 10.1017/S1431927614013658

Toledano, M., Cabello, I., Vílchez, M.A., Fernández, M.A., Osorio, R., 2014c. Surface microanalysis and chemical imaging of early dentin remineralization. Microsc. Microanal. 20, 245-256. DOI: 10.1017/S1431927613013639

Toledano, M., Nieto-Aguilar, R., Osorio, R., Campos, A., Osorio, E., Tay, F.R., Alaminos, M., 2010. Differential expression of matrix metalloproteinase-2 in human coronal and radicular sound and carious dentine. J. Dent. 38, 635-640. DOI: 10.1016/j.jdent.2010.05.001

Toledano, M., Osorio, E., Aguilera, F.S., Sauro, S., Cabello, I., Osorio, R., 2014a. In vitro mechanical stimulation promoted remineralization at the resin/dentin interface. J. Mech. Behav. Biomed. Mater. 30, 61-74. DOI:10.1016/j.jmbbm.2013.10.018

Toledano, M., Sauro, S., Cabello, I., Watson, T., Osorio, R., 2013. A Zn-doped etch-and-rinse adhesive may improve the mechanical properties and the integrity at the

bonded-dentin interface. Dent. Mater. 29, e142-e152. DOI: 10.1016/j.dental.2013.04.024

Tosi, G., Balercia, P., Conti, C., Ferraris, P., Giorgini, E., Mucio, L.L., Sabbatini, S., Stramazzotti, D., Rubini, C., 2011. Microimaging FT-IR of head and neck tumors. V. Odontogenic cystic lesions. Vib Spectrosc 57, 140-147. DOI: 10.1016/j.vibspec.2011.06.006

Vanna, R., Ronchi, P., Lenferink, A.T., Tresoldi, C., Morasso, C., Mehn, D., Bedoni, M., Picciolini, S., Terstappen, L.W., Ciceri, F., Otto, C., Gramatica, F., 2015. Label-free imaging and identification of typical cells of acute myeloid leukaemia and myelodysplastic syndrome by Raman microspectroscopy. Analyst 140, 1054-1064. DOI: 10.1039/c4an02127d

Wang, C., Wang, Y., Huffman, N.T., Cui, C., Yao, X., Midura, S. Midura, R.J., Gorski, J.P., 2009. Confocal laser Raman microspectroscopy of biomineralization foci in UMR 106 osteoblastic cultures reveals temporally synchronized protein changes preceding and accompanying mineral crystal deposition. J. Biol. Chem. 284, 7100-7113. DOI: 10.1074/jbc.M805898200

Wang, Y., Spencer, P., 2003. Hybridization efficiency of the adhesive/dentin interface with wet bonding. J. Dent. Res. 82, 141-145. DOI: 10.1177/154405910308200213

Wang, Y., Spencer, P., Walker, M.P., 2007. Chemical profile of adhesive/caries-affected dentin interfaces using Raman microspectroscopy. J. Biomed. Mater. Res. A. 81, 279-286. DOI: 10.1002/jbm.a.30981

Xu Y., Wu J., Wang H., Li H., Di N., Song L., Li S., Li D., Xiang Y., Liu W., Mo X., Zhou Q., 2013. Fabrication of electrospun poly (L-lactide-co-ε-caprolactone)/collagen nanoyarn network as a novel, three-dimensional,

macroporous, aligned scaffold for tendon tissue engineering. Tissue Eng Part C Methods. 19, 925-936. DOI: 10.1089/ten.TEC.2012.0328

Xu, C., Wang, Y., 2011. Cross-linked demineralized dentin maintains its mechanical stability when challenged by bacterial collagenase. J. Biomed. Mater. Res. B Appl. Biomater. 96, 242-248. DOI: 10.1002/jbm.b.31759

Xu, C., Wang, Y., 2012. Collagen cross linking increases its biodegradation resistance in wet dentin bonding. J Adhes Dent.14, 11-18. DOI: 10.3290/j.jad.a21494.

Yoshiyama, M., Urayama, A., Kimochi, T., Matsuo, T, Pashley, D.H., 2000. Comparison of conventional vs self-etching adhesive bonds to caries-affected dentin. Oper. Dent. 25, 163-169.